

Instituto Tecnológico y de Estudios Superiores de Monterrey

Campus Monterrey

School of Engineering and Sciences



Surface tension analysis and its effect on the coating of CNT structures for electrical applications

A thesis presented by

Jafet Nahir Arano Mata

Submitted to the
School of Engineering and Sciences
in partial fulfillment of the requirements for the degree of

Master of Science

in

Manufacturing Systems

Monterrey Nuevo León, February, 2020

Instituto Tecnológico y de Estudios Superiores de Monterrey

Campus Monterrey

School of Engineering and Sciences

The committee members, hereby, certify that have read the thesis presented by Jafet Nahir Arano Mata and that it is fully adequate in scope and quality as a partial requirement for the degree of Master of Science in Manufacturing Systems.

Dr. Jaime Bonilla Ríos
Tecnológico de Monterrey
Principal Advisor

Dr. Enrique V. Barrera
Rice University
Co-advisor

Dr. Laura Romero apellido 2
Tecnológico de Monterrey
Committee Member?????

Dr. Rubén Morales Menéndez
Dean of Graduate Studies
School of Engineering and Sciences

Monterrey Nuevo León, February, 2020

DECLARATION OF AUTHORSHIP

I, Jafet Nahir Arano Mata, declare that this dissertation titled, Surface tension analysis and its effect on the coating of CNT structures for electrical applications and the work presented in it are my own. I confirm that:

- This work was done wholly or mainly while in candidature for a research degree at this University.
- Where any part of this dissertation has previously been submitted for a degree or any other qualification at this University or any other institution, this has been clearly stated.
- Where I have consulted the published work of others, this is always clearly attributed.
- Where I have quoted from the work of others, the source is always given. With the exception of such quotations, this dissertation is entirely my own work.
- I have acknowledged all main sources of help.
- Where the dissertation is based on work done by myself jointly with others, I have made clear exactly what was done by others and what I have contributed myself.

Jafet Nahir Arano Mata
Monterrey, Nuevo León, March, 2020

DEDICATION

ACKNOWLEDGEMENTS

I wish to acknowledge:

- _____
- _____
- _____
- _____
- _____
- _____
- _____

**Surface tension analysis and its effect on the coating of CNT structures
for electrical applications**

By

Jafet Nahir Arano Mata

Abstract

To study the performance and interactions (insulation, adhesion, conductivity and wettability) of different polymeric coatings on carbon nanotube (CNT) fibers with the objective of making "CNT electrical wires", CNT film (Buckypaper) was used as an approximation because of their advantage of being easier to make at a laboratory scale and also shared similarities such as porosity, surface structure and carbon nature.

The Buckypaper (BP) was prepared by filtering a sonicated solution of single-walled carbon nanotubes and N,N-Dimethylformamide through a polytetrafluoroethylene (PTFE) membrane of 0.45 μm pore size. These were later coated with a thin film of insulating varnish, red enamel, polyethylene wax and epoxy resin.

Tested with scanning electron microscopy, x-ray photoelectron spectroscopy, nitrogen physisorption and raman spectroscopy, the CNT diameter and quality, BP composition, porosity % and pore distribution was determined.

Through contact angle and liquid surface tension measurements, the surface free energy of the BP and interfacial surface tension with the coatings was calculated. With those, adhesion and wettability parameters were obtained, with epoxy resin having the better wetting interaction and red enamel having the best adhesion interaction.

Finally, conductivity was tested with the Van Der Pauw method, with insulating varnish and red enamel having the smallest conductivity decrease 1 day after coating ($\approx 17\%$) and epoxy resin the highest (68.72%).

Contents

List of Tables	10
List of Figures	15
1 Introduction	16
1.1 Introduction	16
2 Materials and methodology	19
2.1 Carbon nanotubes and coating materials	19
2.2 Carbon nanotube film	19
2.3 Characterization	21
2.3.1 Scanning Electron Microscopy (SEM)	22
2.3.2 Raman Spectroscopy	22
2.3.3 X-ray Photoelectron Spectroscopy	24
2.3.4 Nitrogen Physisorption	25
2.3.5 Wettability	30
2.4 Conductivity measurements	33
3 Results and discussion	36
3.1 Materials characterization	36
3.1.1 Raman Spectroscopy	36
3.1.2 X-ray Photoelectron Spectroscopy	40

3.1.3	Nitrogen Physisorption	42
3.1.4	Wettability	54
3.1.5	Conductivity	76
4	Conclusions	81

List of Tables

2.1	Specifications of the selected coatings.	19
2.2	Characterization scheme for the Buckypaper (BP).	21
2.3	Binding energies of common chemical states of carbon. Obtained from [1].	25
2.4	Binding energies of common chemical states of oxygen. Obtained from [2].	25
2.5	Binding energies of common chemical states of nitrogen. Obtained from [3].	25
3.1	Values where some raman features are found on Figure 3.1a.	37
3.2	Values where some raman features are found on Figure 3.2a.	38
3.3	Values where some raman features are found on Figure 3.3a.	39
3.4	Values for certain regions on Figure 3.5.	40
3.5	BET plot data points.	44
3.6	Data obtained from physisorption results (pore width is the pore with the highest mode).	50
3.7	Thickness measurements on 20 different spots of a BP.	51
3.8	Porosity calculation of the BP from the DFT and BJH results.	52
3.9	(Theoretical porosity calculation of the BP using reported SWCNT densities.	53
3.10	Polar and dispersive surface energy components of the test liquids. Extracted from [4].	57

3.11 Contact Angle (CA) values for High Performance Liquid Chromatography (HPLC) grade water, glycerol and diiodomethane droplets on BP.	58
3.12 Surface tension of the coating-air interface.	63
3.13 Initial and final contact angles (CA_0 and CA_{dry}) measured from 3 drops of insulating varnish on 3 BPs.	64
3.14 Initial and final contact angles (CA_0 and CA_{dry}) measured from 3 drops of red enamel on 3 BPs.	66
3.15 Initial and final contact angles (CA_0 and CA_{dry}) measured from 3 drops of epoxy resin on 3 BPs.	68
3.16 Average initial and final contact angles (CA_0 and CA_{dry}) for insulating varnish, red enamel and epoxy resin.	70
3.17 Contact angle calculations with the Cassie-Baxter model (Equation 3.4).	72
3.18 Wetting parameters (mJ/m^2) calculated for red enamel, insulating varnish and epoxy resin.	73
3.19 Curing conditions for all coatings.	77
3.20 Resistivities (ρ) of samples that were coated, where day 0 is the measurement for the uncoated sample and from day 1 on is the coated and cured sample. S1, S2 and S3 are samples 1, 2 and 3 of each coating.	78
3.21 Resistivities (ρ) of uncoated control samples.	78
3.22 Conductivities (σ) of uncoated control samples.	79
3.23 Conductivities (σ) of samples that were coated, where day 0 is the measurement for the uncoated sample and from day 1 on is the coated and cured sample.	80
3.24 Average conductivity change ($\Delta \sigma$) of each set of 3 samples from their first day of measurement (Day 0).	80

List of Figures

1.1	CNT cable considerations.	18
2.1	Filtration setup.	20
2.2	Buckypaper fixed to glass (a), and Buckypaper peeled from PTFE membrane (b).	21
2.3	FEI Quanta 400 Environmental SEM.	22
2.4	Tilt stage installed on FEI Quanta 400 Environmental SEM.	22
2.5	Raman spectrum from a Raman Spectroscopy performed with a 785 nm laser on a BP, with features labeled on the spectra (RBM, D-band, G-band and G'-band).	23
2.6	The G-band for highly oriented pyrolytic graphite (HOPG), one semi-conducting SWCNT, and one metallic SWCNT. Extracted from [5].	24
2.7	Classification of physisorption isotherms. Extracted from [6].	26
2.8	Pore with adsorbed gaseous N ₂ layer(s) on wall filled with N ₂ liquid condensate.	29
2.9	KRÜSS DSA100S.	30
2.10	Wetting behavior of solid substrates: (a) Young, (b) Wenzel, (c) Cassie, (d) intermediate state between Wenzel and Cassie regimes. Extracted from [7].	30
2.11	Pendant drop of red enamel (heavy phase) suspended in air (light phase), where the radii of the horizontal (green) and vertical (blue) circles of curvature define the surface curvature at point P.	32
2.12	Pendant drop with curvature affected by gravity.	33
2.13	Keithley 2400 Source meter.	34

2.14 Representation of the directions at which RA and RB are measured.	34
3.1 Raman spectroscopy at 785nm beam of a BP at three different spots, with a 500 counts displacement between each (a), and normalized graph with a .015 normalized intensity displacement each (b). RBM region zoomed in (a).	38
3.2 Raman spectroscopy at 633nm beam of a BP at three different spots, with a 500 counts displacement between each (a), and normalized graph with a .015 normalized intensity displacement each (b). RBM region zoomed in (a).	39
3.3 Raman spectroscopy at 532nm beam of a BP at three different spots, with a 500 counts displacement between each (a), and normalized graph with a .015 normalized intensity displacement each (b). RBM region zoomed in (a).	40
3.4 X-ray Photoelectron Spectroscopy of a BP.	41
3.5 Visual representation of a C1s region deconvolution from XPS data. Extracted from [8].	41
3.6 Isotherm graph for the adsorption (lower line) and desorption (higher line) of nitrogen with all the data (a), and removing the highest adsorption/desorption value (b).	42
3.7 Classification of hysteresis loops. Extracted from [6].	43
3.8 Isotherm plot for the CNT fibers. Retrieved from [9].	43
3.9 BET plot generated from the BP physisorption isotherm and its equation (linear regression).	45
3.10 The cumulative volume that pores of the same width amount to per nm (a) and it's total volume contribution per gram of BP (b) by the DFT.	45
3.11 Distribution of the total pore volume by the total pore volume of all different pore widths by the DFT in a histogram, starting from a width of 1.05 nm and grouping every 0.2 nm increase.	46
3.12 The cumulative pore volume formed by adding the total pore volume of all pore widths by the DFT.	46
3.13 The cumulative surface area that pores of the same width amount to per nm (a) and it's total surface area contribution per gram of BP (b) by the DFT.	47

3.14 The cumulative surface area by the DFT.	47
3.15 The cumulative volume that pores of the same width amount to per nm using all isotherm desorption values(a) and it's total volume contribution per gram of BP (b). The cumulative volume that pores of the same width amount to per nm omitting the highest desorption value (c) and it's total volume contribution per gram of BP (d), all obtained with the BJH method.	48
3.16 The cumulative pore volume formed by adding the total pore volume of all pore widths calculated by the BJH theory using all desorption values (a) and omitting the highest desorption value (b) by the BJH method.	49
3.17 The cumulative surface area when using all desorption values (a) and when omitting the highest desorption value, both obtained through the BJH theory.	49
3.18 The cumulative surface area that pores of the same width amount to per nm using all isotherm desorption values(a) and it's total surface area contribution per gram of BP (b). The cumulative surface area that pores of the same width amount to per nm omitting the highest desorption value(c) and it's total surface area contribution per gram of BP (d), all obtained with the BJH theory.	50
3.19 Side view of a BP at a 1349x magnification with a SEM.	52
3.20 Representation of a SWCNT as a cylinder. Extracted from [10]. . .	54
3.21 Droplet of water on top of a BP.	55
3.22 MWCNT fiber surface taken at Rice University by Dr. Lucas at a 60,000x magnitude and 10.2 mm working distance (WD) (a) and surface of a SWCNT buckypaper taken at ITESM at a x40,000 magnitude and 5 mm WD (b).	55
3.23 Graph obtained to calculate Owens-Wendt model parameters.	59
3.24 A BP with single drops of water applied through most of the surface.	60
3.25 A drop of water on the surface of a BP, with contact angle measured for 35 minutes.	60
3.26 Measurements on a drop of water on top of a BP.	61
3.27 Change in contact angle on a graphene layer. Extracted from [4]. . .	62
3.28 Measurement of surface tension on the red enamel-air interface through the pendant drop method.	63

3.29 Measurement of surface tension on the epoxy-air interface through the pendant drop method.	63
3.30 Measurement of surface tension on the insulating varnish-air interface through the pendant drop method.	64
3.31 Measurement of the contact angle of a drop of varnish on a BP through the young-Laplace fitting 5 minutes after it was placed.	65
3.32 Measurement of the contact angle of a drop of insulating varnish on a BP through the young-Laplace fitting for 5 minutes after it was placed on 3 different BPs (CS1-CS3) three drops each.	65
3.33 Measurement of the contact angle of a drop of insulating varnish on a BP through the young-Laplace fitting for 40 minutes after it was placed on 3 different BPs (CS1-CS3).	66
3.34 Contact angle change on a drop of red enamel on top of a BP at minutes 0, 5 and 40 from when it was dropped.	67
3.35 Measurement of the contact angle of a drop of red enamel on a BP through the young-Laplace fitting for 5 minutes after it was placed on 3 different BPs (CS1-CS3) three drops each.	67
3.36 Measurement of the contact angle of a drop of red enamel on a BP through the young-Laplace fitting for 40 minutes after it was placed on 3 different BPs (CS1-CS3).	68
3.37 Measurement of the contact angle of a drop of epoxy resin on a BP through the young-Laplace fitting 5 minutes after it was placed.	69
3.38 Measurement of the contact angle of a drop of epoxy resin on a BP through the young-Laplace fitting for 5 minutes after it was placed on 3 different BPs (CS1-CS3) three drops each.	69
3.39 Measurement of the contact angle of a drop of epoxy resin on a BP through the young-Laplace fitting for 40 minutes after it was placed on 2 different BPs (CS2 and CS3).	70
3.40 Contact angle profile for 40 minutes for all three coatings from Figures 3.33, 3.36 and 3.39.	71
3.41 Infiltration of a liquid in the pores of a porous structure. Extracted from [11].	72
3.42 Image of the interface formed from a BP coated with red enamel (coated side is the upper layer) at 300x (a) and 2400x (b) magnitudes.	74

3.43 Image of the interface formed from a BP coated with insulating varnish (coated side is the lower layer) at a 1500x magnitude.	75
3.44 Image of the interface formed from a BP coated with epoxy resin (coated side is the upper layer) at 15000x (a) and 30000x (b) magnitudes.	75
3.45 Image of the interface formed from a BP coated with Polyethylene wax (coated side is the lower layer) at 1500x (a) and 15000x (b) magnitudes.	76
3.46 Conductivity measurement setup before coating.	76
3.47 Buckypaper connected to copper tape through silver paint. The Buckypaper has 3 fused drops of red enamel on the center.	77
3.48 Representation of the cross pattern in which the coating was applied.	77
3.49 Conductivity measurement setup after coating.	78

Chapter 1

Introduction

1.1 Introduction

Since their discovery in 1991, carbon nanotubes (CNTs) have been widely studied due to their mechanical, optical, chemical, and electronic properties, allowing a wide variety of applications [12]. However, it wasn't until the last decade that most of those incredible properties were retained when scaling to produce macroscopic CNT structures, such as fibers or films [13].

New CNT-polymer composites were materials that would enhance performance in aircrafts, automobiles, civil infrastructures, marine and sporting goods [14]. Creating also opportunities for electrical heating applications [15], polarization [16], electrical energy harvesting [17] and inductors [18].

One obstacle for these applications, is that properties depend on the inherent properties of the CNTs (number of walls, aspect ratio, quality, chirality), and having a process where you can control all those factors and get always the exact same CNTs is very complicated. Also, the cost of CNTs is still elevated, depending on the application. Out of the most expensive commercial CNTs, 98% pure semiconducting single-walled carbon nanotubes (SWCNTs) cost around 629 dollars per gram [19], while 98% pure metallic SWCNTs can go up to 941 dollars per gram [20].

Nonetheless, the biggest advantage that CNTs have over other materials is their relatively low density.

Values as low as 1.74 g/cm^3 for isolated and acid treated SWCNTs at room temperature [21] have been reported, which rival the 8.96 g/cm^3 for copper [22] and allow the reaching of higher specific conductivity.

The highest reported conductivity for undoped CNT fiber is $8.5 \times 10^6 \text{ S/m}$ [13], while for copper is 5.88×10^7 and for Aluminum is 3.16×10^7 [22]. However, iodine doping of CNT fiber has shown an increase in conductivity of raw Double walled-CNT fiber with

diameters in the range of 2-3 nm, by penetrating the interstitial space between the tubes and forming an intercalated structure [23]. Added to their already low density, CNT fibers reach higher specific conductivity than copper or aluminum. Specific conductivity for those reported CNT fibers is 19.6 kSm²/kg [23], while copper and aluminum report 6.59 kSm²/kg and 11.8 kSm²/kg respectively [22].

With Projections indicating that in 2019 and 2020, world stocks of refined copper, will suffer a deficit of about 190,000 and 250,000 thousand metric tons respectively [24], finding economically viable ways to process CNT fiber alternatives is becoming relevant.

In these latest new magnetic and electrical features, investigation on effective insulation of the CNT structures is of vital importance, and the key to achieve it, is the study of coatings.

Making electrical applications possible by proper thermal and electrical insulation, increasing the safe to touch areas and preventing bare wiring to touch another wire, while not altering conductivity of the material and providing a flexible and anti-corrosive layer is what makes coatings so important.

The second obstacle to overcome, and the focus of this thesis, is that CNT structures have porous structures [25][23][26][9], which open physical interactions between the CNTs and coatings that now must be considered, different from the coating of metals, and an important parameter to study these interactions is wettability.

CNT materials usually present hydrophobic behavior. However, surface modification studies such as Photo-initiated chemical vapour deposition (PICVD) using syngas have shown that wettability can be altered [27]. Also, functionalization allows for a better bonding with a wider variety of materials.

The possibility of using the CNT fibers for different electrical applications has been proven before. A USB cable consisting of CNT fibers and a PVA coating was successfully used for data or power transmission within USB 2.0 capabilities [26].

This thesis studies the interactions that involve the coating of a porous CNT film (Buckypaper) as an approach to CNT wires, considering the wetting aspects and the effect it has in the conductivity while comparing different coating materials.

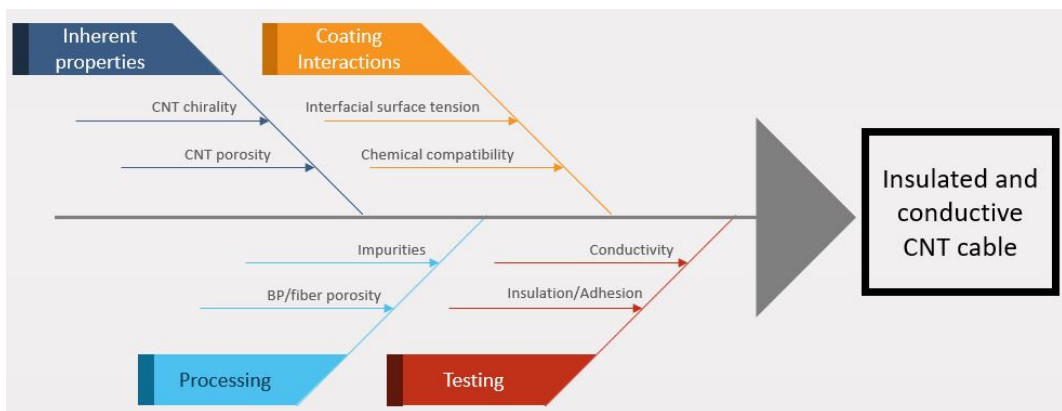


Figure 1.1: CNT cable considerations.

Chapter 2

Materials and methodology

2.1 Carbon nanotubes and coating materials

Single-walled carbon nanotubes from Rice University, produced by the high-pressure carbon monoxide (HiPCO) method were processed into film (Buckypaper), and tested with four different coating materials. For the coating materials, the selected insulating materials were:

- Glyptal® 1201 Red Enamel (Xylene solvent, 60% weight of solids).
- Glyptal® 1202 Insulating Varnish (Xylene solvent, 50% weight of solids).
- 635 Thin Epoxy Resin and 635 Epoxy Hardener from USComposites® in a 2:1 ratio.
- Epolene® wax from Westlake Chemicals.

Table 2.1: Specifications of the selected coatings.

Coating	Heat resistance (°C)	Viscosity (cp)	Specific gravity
Insulating Varnish	145	230 @25°C	0.98 @25°C
Red Enamel	135	325 @25°C	1.17 @25°C
Epoxy system	150	600 @25°C	0.9857 @25°C
PE wax	-	-	-

2.2 Carbon nanotube film

The methodology for the making of Buckypaper is as follows:

A filtration set up consisting of a 1000 ml vacuum filtering flask sealed with a rubber stopper, a glass support base, a polytetrafluoroethylene membrane filter with a 47 mm diameter and 0.45 μm pore size from Sartorius Stedim Biotech GmbH, a 300 ml glass funnel and a clamp is built as the one in Figure 2.1.



Figure 2.1: Filtration setup.

First, a solution of .0540 g of SWCNTs and 100 ml of N,N-Dimethylformamide obtained from Sigma Aldrich is prepared. The solution is then sonicated for 45 min with a tip sonicator with 45% amplitude and a pulse rate of 2 seconds on and 2 seconds off.

As soon as the sonication is over, 50 ml of isopropanol are poured on the filtering set up to wet the membrane and allow the CNT solution to filter. After the isopropanol completely filters, 50 ml of the CNT solution are poured and allowed to sit for 15 minutes. After that time, the membrane is taken off the set up.

To remove the remaining N,N-Dimethylformamide there are two ways, depending on the desired sample:

- a) To get the Buckypaper (BP) to stick on a glass slide (Figure 2.2a), it's carefully peeled from the membrane and placed on the slide. Afterwards, it's placed in the oven at 80°C for 30 minutes.
- b) To place the membrane with the Buckypaper in a petri dish, and then in the oven at 80°C for 30 minutes to remove any remaining solvent. The Buckypaper is then carefully peeled from the membrane (Figure 2.2b).

BP stuck in glass was used on contact angle measurements (method a), while peeled BP (method b) was used on XPS, raman spectroscopy, nitrogen adsorption-desorption, SEM imaging and in the conductivity setup.

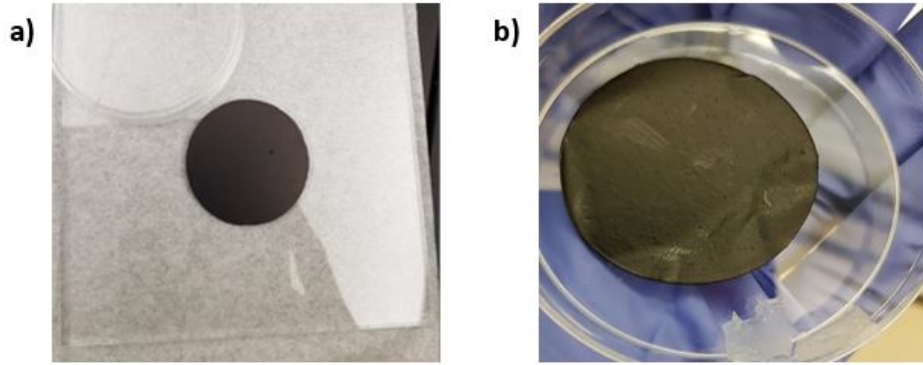


Figure 2.2: Buckypaper fixed to glass (a), and Buckypaper peeled from PTFE membrane (b).

2.3 Characterization

The BP was analyzed through different equipment in order to obtain information such as porosity, surface free energy, specific surface area, nanotube quality, chirality and diameter.

Table 2.2: Characterization scheme for the Buckypaper (BP).

Methodology	Characterization	Objective
SEM	BP surface, BP-coating Interface	CNT fiber vs BP surface, Interface analysis
Raman Spectroscopy	SWCNT diameter, quality and chirality	SWCNT characterization
XPS	Oxygen, Iron, Nitrogen	Look for solvent remains, oxidation and impurities
Nitrogen physisorption	Surface area, Pore distribution	Porosity
Contact angle (CA) measurement	BP-HPLC H ₂ O CA, BP-glycerol CA, BP-CH ₂ I ₂ CA, BP-coating CA	BP surface free energy
Pendant drop liquid-air surface tension	Coating-air surface tension	With BP surface free energy and BP-coating CA calculate interface surface tension

2.3.1 Scanning Electron Microscopy (SEM)

Scanning Electron Microscopy (SEM) Imaging for coated and uncoated BP samples was performed on a FEI Quanta 400 Environmental SEM. The only exception is Figure 3.22b, which was taken at ITESM with a ZEISS EVO MA 25 SEM (no field emission).



Figure 2.3: FEI Quanta 400 Environmental SEM.

For the lateral imaging of the samples, the tilt stage was used (Figure 2.4).

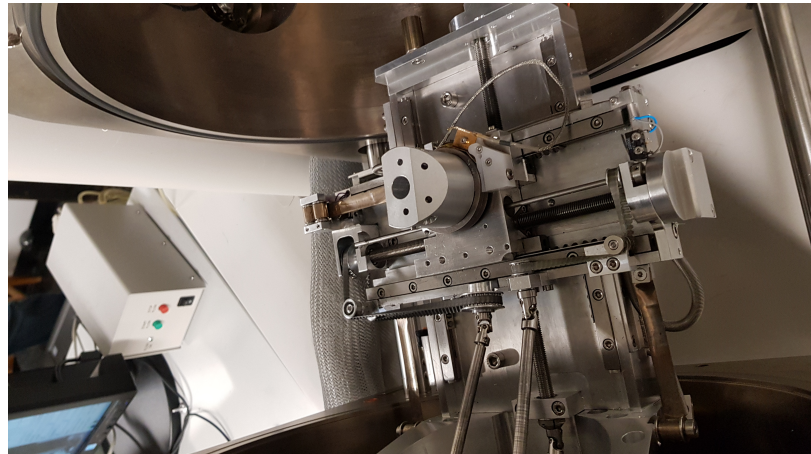


Figure 2.4: Tilt stage installed on FEI Quanta 400 Environmental SEM.

2.3.2 Raman Spectroscopy

Raman Spectroscopy is a methodology based on a light scattering technique, where a molecule scatters incident light from a high intensity laser light source. A small amount of that light is scattered at different wavelengths (Raman scattering), which depend on the chemical structure of the analyte.

The scattering is represented in a spectrum, where a number of peaks show the intensity and wavelength position of the Raman scattered light. Each peak corresponds to a specific chemical bond vibration, and from them different information can be obtained depending on the analyzed material [28].

For sp^2 nanocarbons such as graphene or carbon nanotubes, Raman spectroscopy can give information about defects and other crystal disorders, nanotube diameter, curvature, chirality, and metallic vs semiconducting behavior [29]. This mainly through the analysis of four main features on the Raman Spectrum (G-band, Radial Breathing Mode (RBM), Dispersive G'-band and Disorder Induced D-Band. Figure 2.5).

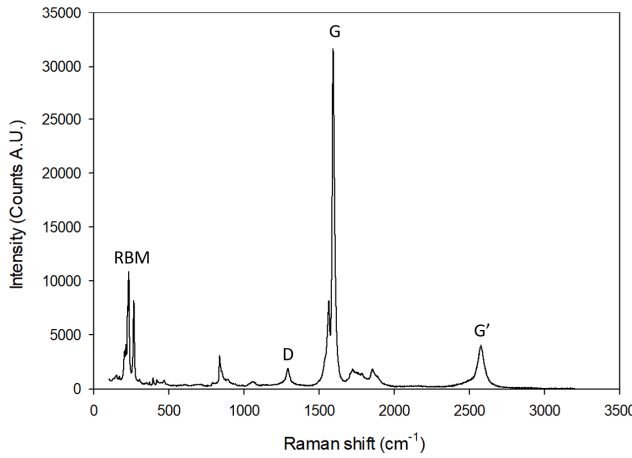


Figure 2.5: Raman spectrum from a Raman Spectroscopy performed with a 785 nm laser on a BP, with features labeled on the spectra (RBM, D-band, G-band and G'-band).

The RBM feature correspond to the vibration of the C atoms in the radial direction. When there is a presence of SWCNTs with diameters (d_t) in the range of 0.7-2 nm, this feature appears in frequencies (w_{RBM}) between $120-350\text{ cm}^{-1}$. CNT diameter distribution is characterized through Equation 2.1, where A and B are parameters determined experimentally [30].

$$w_{RBM} = A/d_t + B \quad (2.1)$$

In a study [31], $A = 234\text{ cm}^{-1}\text{nm}$ and $B = 10\text{ cm}^{-1}$ were found for SWCNT bundles with $d_t = 1.5 \pm 0.2\text{ nm}$.

The G-band is associated with stretching of the C-C bonds, making it sensitive to strain effects. Curvature effects, such as the ones in SWCNTs, and phonon wave vector confinement along the SWCNT circumferential direction cause multiple peaks to appear in the G-band spectrum [30]. This band is important for distinguishing between metallic and semiconducting SWCNTs through strong differences in their Raman lineshape (Figure 2.6), mainly because of their different coupling between electrons and phonons. In metallic systems, the process at which electron-hole pairs

are created through phonon excitation is stronger than in semiconducting systems as this process depends on the chiral angle and on quantum confinement effects [32].

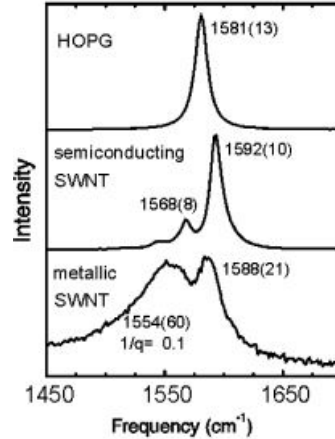


Figure 2.6: The G-band for highly oriented pyrolytic graphite (HOPG), one semiconducting SWCNT, and one metallic SWCNT. Extracted from [5].

The disorder induced D-band intensity is a measurement of the defects on carbon nanotubes. Thus, the G/D intensity ratio is often used as an indicator of the quality of CNTs.

Raman spectroscopy was performed using a Renishaw inVia confocal Raman microscope equipped with 3 lasers (532nm, 633nm, and 785nm).

2.3.3 X-ray Photoelectron Spectroscopy

X-ray Photoelectron Spectroscopy (XPS) analysis was performed using a PHI Quanta XPS on uncoated Buckypaper.

XPS is a technique used to measure the elemental composition, chemical state, empirical formula and electronic state of the elements within a material. Its spectrum is obtained by irradiating a solid surface with a beam of X-rays while simultaneously measuring the electrons emitted from the top 1-10 nm of the material being analyzed and the kinetic energy. To build the spectrum, the ejected electrons are counted over a range of electron kinetic energies. Peaks appear in the spectrum from atoms emitting electrons of a particular characteristic energy. Through the analysis of energies and intensities of the peaks, the characterization above described is obtained.

The three main elements to identify on the BP are carbon, nitrogen and oxygen.

Table 2.3: Binding energies of common chemical states of carbon. Obtained from [1].

Chemical state	Binding energy C1s/eV
C-C	284.8
C-O-C	~286
O-C=O	~288.5

Table 2.4: Binding energies of common chemical states of oxygen. Obtained from [2].

Chemical state	Binding energy O1s/eV
Metal oxides	529-530
Metal carbonates	531.5-532
Alumina	531.1
SiO ₂	532.9
Organic C=O	531.5-532
Organic C-O	~533
O-F _x	~535

Table 2.5: Binding energies of common chemical states of nitrogen. Obtained from [3].

Chemical state	Binding energy N1s/eV
Metal nitrides	~397
NSi ₃	398
NSi ₂ O	399.9
NSiO ₂	402.5
C-NH ₂	~400
Nitrate	>405

2.3.4 Nitrogen Physisorption

Gas adsorption-desorption is very useful when characterizing porous materials, with porosity information obtained through different methods from the adsorption-desorption isotherm obtained by plotting the amount of gas adsorbed against the equilibrium relative pressure. These isotherms are classified in 6 main types by the International Union of Pure and Applied Chemistry (IUPAC) [6], as shown in Figure 2.7.

The Brunauer-Emmett-Teller (BET) method [33] is the most common way of estimating the surface area of porous materials, which can be regarded as the effective area available for the adsorption of an adsorptive.

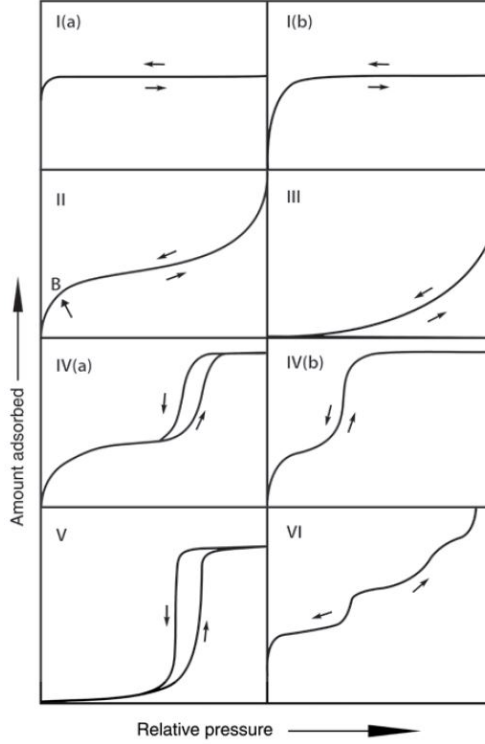


Figure 2.7: Classification of physisorption isotherms. Extracted from [6].

The first step of the method is to transform the physisorption isotherm into a BET plot to calculate the sufficient weight of adsorbate to cover the surface with a complete monolayer of molecules per gram of sample (W_m).

The BET plot is constructed with the linear behavior between $\frac{1}{W(p^o/p - 1)}$ and p/p^o when using certain range of values from the isotherm (commonly $0.05 < p/p^o < 0.3$ for type II and IVa isotherms). This plot is described by Equation 2.2, where 'W' is the weight of gas adsorbed at a particular adsorbate pressure 'p', ' p/p^o ' is the result of dividing 'p' by the saturated pressure of the same adsorbate ' p^o ', and 'C' is a parameter related to the energy of monolayer adsorption.

$$\frac{1}{W(p^o/p - 1)} = \frac{1}{W_m C} + \frac{C - 1}{W_m C} (p/p^o) \quad (2.2)$$

With Equation 2.2, W_m and C are calculated using Equations 2.3 and 2.4 respectively.

$$W_m = \frac{1}{slope + intercept} \quad (2.3)$$

$$C = 1 + \frac{slope}{intercept} \quad (2.4)$$

The BET surface area (A_s) is then obtained with Equation 2.5, where 'L' is the avogadro constant, 'M' is the molecular weight of the adsorbate gas and ' σ_m ' is the average area occupied by the adsorbate molecule in the complete monolayer (molecular cross-sectional area). For Nitrogen at 77K, σ_m is usually considered as 0.162 nm² (assuming a closed-packed monolayer) [6].

$$A_s = \frac{W_m * L * \sigma_m}{M} \quad (2.5)$$

For the characterization of the pores on a porous material, the Density Functional Theory (DFT) and the Barret-Joyner-Halenda (BJH) methods were used.

The DFT is based on calculating equilibrium density profiles of a fluid adsorbed on the surface and in the pores from which properties such as the adsorption/desorption isotherm can be derived.

The Non-Local Density Functional Theory (NLDFT) studies in particular the oscillating density profiles at the solid-fluid interface that are characteristic of narrow micropores. These density profiles refer to coexisting gas-liquid states of a fluid in a slit-like pore.

As indicated above, the Non-Local Density Functional Theory (NLDFT) and the Grand Canonical Monte Carlo simulation (GCMC) methods correctly describe the local fluid structure near curved solid walls; adsorption isotherms in model pores are determined based on the intermolecular potentials of the fluid-fluid and solid-fluid interactions. The relation between isotherms determined by these microscopic approaches and the experimental isotherm on a porous solid can be interpreted in terms of a Generalized Adsorption Isotherm (GAI) equation:

$$N\left(\frac{p}{p^o}\right) = \int_{W_{MAX}}^{W_{MIN}} N\left(\frac{p}{p^o}, W\right) f(W) d(W) \quad (2.6)$$

Where:

$N\left(\frac{p}{p^o}\right)$ = Experimental adsorption isotherm data.

W = pore width.

$N\left(\frac{p}{p^o}, W\right)$ = isotherm on a single pore of width 'W'.

$f(W)$ = pore size distribution function.

This equation assumes that the total isotherm consists of a number of individual 'single pore' isotherms multiplied by their relative distribution ' $f(W)$ ' over a range of different pore sizes. The $N\left(\frac{p}{p^o}\right)$ isotherms are obtained by the DFT, and the pore size

distribution is then derived by solving Equation 2.6 numerically [34].

The Barrett-Joyner-Halenda (BJH) method is used for characterization of the pores on a porous solid that has the presence of mesopores and macropores. This methodology consists of a modification of the Kelvin equation (Equation 2.7), which assumes multilayer formation in parallel to capillary condensation.

$$\ln\left(\frac{p}{p^0}\right) = \frac{2\gamma V}{r_k RT} \cos\theta \quad (2.7)$$

Where:

p = pressure of adsorbate.

p^0 = saturated pressure of adsorbate.

γ = liquid surface tension.

r_k = mean radius of curvature for the liquid meniscus.

R = gas constant.

T = temperature.

θ = contact angle between the solid and condensed phase.

When using values for N_2 and solving for r_k , the formula is reduced to:

$$r_k = \frac{4.15}{\log(p^0/p)} [A^o] \quad (2.8)$$

The actual pore radius is not r_k , since there is also adsorption on the walls of the pore prior to condensation (Figure 2.8).

The actual pore radius " r_p " is obtained with Equation 2.9.

$$r_p = r_k + t \quad (2.9)$$

Where:

r_p = actual pore radius.

t = thickness of the adsorbed layer.

Because of the difficulty on estimating the thickness, an adsorbate evenly distributed

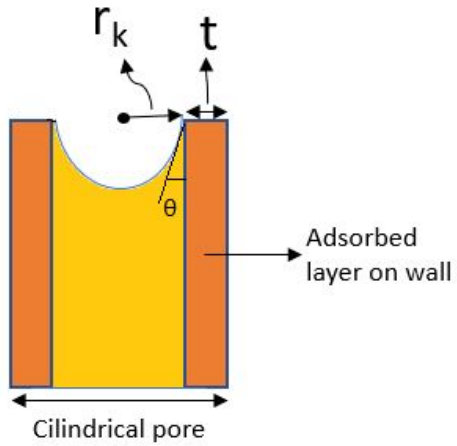


Figure 2.8: Pore with adsorbed gaseous N_2 layer(s) on wall filled with N_2 liquid condensate.

over the surface and a planar surface are assumed.

$$t = \left(\frac{W_a}{W_m} \right) \tau \quad (2.10)$$

Where:

W_a = weight adsorbed.

W_m = weight for monolayer coverage.

τ = thickness of one layer.

For liquid nitrogen $\tau=3.54 \text{ \AA}^\circ$.

The desorption part of the isotherm is preferred for calculations, since it not only represents the mesopore system but also has meniscus development.

Nitrogen physisorption studies were performed using a Quantachrome Novatouch NT1LX-1 instrument. At pressures lower than 25 mtorr, the sample was first degassed with a progressive temperature increase. First, with an increase of $10^\circ\text{C}/\text{min}$ until it reached 60°C and held for an hour. Then, with the same temperature increase rate, raised to 200°C and held for 4 hours.

The physisorption analysis was standard, with a 9mm cell with bulb without filler rod. The leak test lasted 1 minute, with 68 points in adsorption and 54 in desorption.

2.3.5 Wettability

All contact angles were analyzed on a KRÜSS DSA100S using a 21G syringe, based on the sessile drop method, with the KRÜSS ADVANCE software. While the pendant drop method allowed to measure the surface tension of the coatings on a liquid-air interface.



Figure 2.9: KRÜSS DSA100S.

Wettability is the ability of liquids to stay in contact with solid surfaces. One important parameter that shows the effect of wettability in a system is the contact angle (CA). The interpretation of the contact angle on the solid is represented in 4 different theorems (Figure 2.10).

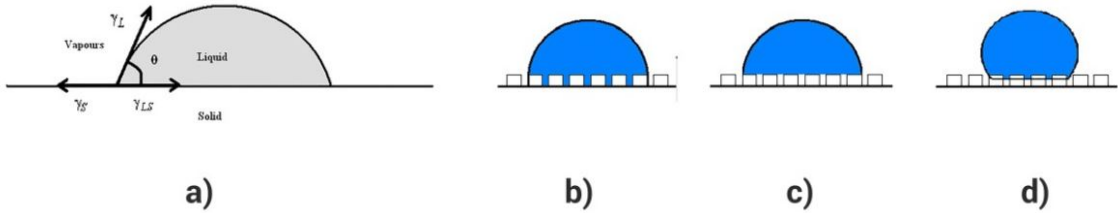


Figure 2.10: Wetting behavior of solid substrates: (a) Young, (b) Wenzel, (c) Cassie, (d) intermediate state between Wenzel and Cassie regimes. Extracted from [7].

The Young's model [35]:

For liquid droplets forming a $\text{CA}(\theta)$ on ideal solid surfaces (flat, perfectly smooth, rigid, chemically homogeneous), Young's equation (Equation 2.11) describes the balance between the surface tension of the solid/vapor (γ_{SV}), the liquid/vapor (γ_{LV}) and the interfacial tension between the solid and the liquid (γ_{LS}).

$$\cos\theta = \frac{\gamma_{SV} - \gamma_{LS}}{\gamma_{LV}} \quad (2.11)$$

The problem with the Young approximation, is that surface roughness is a parameter that also has to be taken into consideration, the three resting models correlate the roughness of the surface with the apparent CA of the liquid.

The Wenzel model [36]:

This model considers a penetration of the liquid on the solid, which creates an apparent contact angle when measured by the Young model. The real and apparent contact angles are related through 'r', which is the ratio of the actual to projected area, caused by the roughness (Equation 2.12). This means there is also an apparent γ_{SV} and γ_{LS} , related to the real values by 'r' the same way as for the CA.

$$\cos\theta_{apparent} = r\cos\theta_{real} \quad (2.12)$$

The Cassie-Baxter model [37]:

This theorem considers that under the liquid droplet, the air is trapped inside the pores. The apparent angle is related to the roughness through equation 2.13, where f_s is the area fraction of the solid on the surface.

$$\cos\theta_{apparent} = -1 + f_s(\cos\theta_{real} + 1) \quad (2.13)$$

The Wenzel and Cassie-Baxter transition:

A transition between the Wenzel and Cassie-Baxter methods can occur when there is a deformation on a spherical droplet, causing the liquid to use some of the space of the air droplets and resulting in a combined state [38]. The resulting threshold value between the states (θ_{th}) is obtained with equation 2.14 [39].

$$\cos\theta_{th} = \frac{f_s - 1}{r - f_s} \quad (2.14)$$

Pendant drop method:

It's an optical method used for determining the interfacial or surface tension of a suspended drop of a heavier liquid within a lighter phase (in this thesis it's a coating-air interface) by using the curvature of the drop.

This tension between phases results in an increased pressure inside the drop. This difference in pressure (Δp) and the interfacial tension are related by the Laplace equation:

$$\Delta p = \sigma \left(\frac{1}{R_1} + \frac{1}{R_2} \right) \quad (2.15)$$

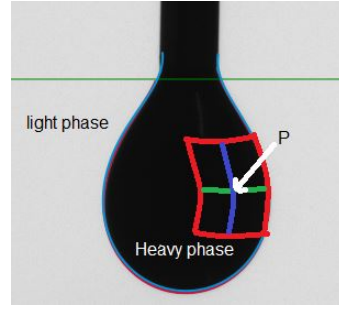


Figure 2.11: Pendant drop of red enamel (heavy phase) suspended in air (light phase), where the radii of the horizontal (green) and vertical (blue) circles of curvature define the surface curvature at point P.

Δp = inner pressure - outer pressure = Laplace pressure.

σ = Interfacial tension.

R_1 = Radius of horizontal circle of the curvature.

R_2 = Radius of vertical circle of the curvature.

The two main forces that define the shape of the drop are gravity and the surface tension. While surface tension makes the drop assume the smallest possible surface area, gravity deforms the drop through the hydrostatic pressure generated by the weight according to Pascal's law, this effect is expressed in Equation 2.16.

$$\Delta p_{Hydro} = \Delta \rho g l \quad (2.16)$$

Δp_{Hydro} = Hydrostatic pressure.

$\Delta \rho$ = Density difference between lighter and heavier phases (gas and liquid).

g = Gravitational acceleration.

l = Vertical point between measuring point and needle opening.

For a pendant drop, both radii of curvature at the lowest point of the drop are the same ($R_1=R_2=R$). For every point above it, $R_2=x/\sin\theta$ (Figure 2.12).

Taking the lowest point of the drop as the initial point results in Equation 2.17.

$$\frac{1}{R_1} + \frac{\sin\theta}{x} = \frac{2}{R} \pm \frac{\Delta \rho g z}{\sigma} \quad (2.17)$$

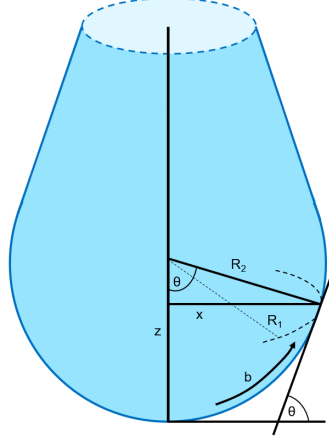


Figure 2.12: Pendant drop with curvature affected by gravity.

To solve the equation, the arc length 'b' of the drop shape is used to obtain through parametrisation a set of three first-order differential equations with three boundary values (Equations 2.18, 2.19 and 2.20).

$$\frac{d\theta}{db} = -\frac{\sin\theta}{x} + \frac{2}{R} \pm \frac{\Delta\rho g z}{\sigma} \quad (2.18)$$

$$\frac{dx}{db} = \cos\theta \quad (2.19)$$

$$\frac{dz}{db} = \sin\theta \quad (2.20)$$

$$0 = x(b=0) = z(b=0) = \theta(b=0)$$

Where 'b' is the arc, function of 'x' and ' θ '.

From the imaging, using greyscale analysis the shape of the drop is determined. Then, a shape parameter 'B factor' or 'b' is varied with numerical methods until a calculated drop shape matches the actual shape. Knowing the shape drop dimensions and the density difference, the surface tension can be obtained.

2.4 Conductivity measurements

The sheet resistance and electrical resistivity measurements were obtained as outlined by the National Institute of Standards and Technology [40], through the Van Der Pauw method.

The sheet resistance is first obtained by the relationship between two different resistances (R_A and R_B), which are the average of the four ways voltage can go in two different directions (Figure 2.14). These were measured using a Keithley 2400 Source meter (Figure 2.13).



Figure 2.13: Keithley 2400 Source meter.

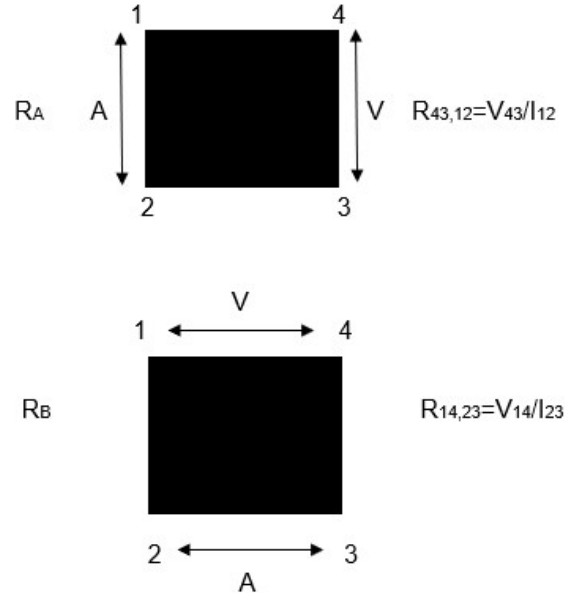


Figure 2.14: Representation of the directions at which R_A and R_B are measured.

$$R_A = (R_{21,34} + R_{12,43} + R_{43,12} + R_{34,21})/4 \quad (2.21)$$

$$R_B = (R_{32,41} + R_{23,14} + R_{14,23} + R_{41,32})/4 \quad (2.22)$$

Sheet resistance (R_s) is then determined using the Van Der Pauw Equation:

$$1 = \exp(-R_A/R_s) + \exp(-R_B/R_s) \quad (2.23)$$

Bulk electrical resistivity of the carbon nanotube film was determined using Equation 2.24:

$$r = R_s d \quad (2.24)$$

Where r is electrical resistivity, R_s is the sheet resistance of the carbon nanotube film, and d is the sample thickness.

Sample thickness was determined with a Vernier caliper.

Chapter 3

Results and discussion

3.1 Materials characterization

Raman spectroscopy, XPS and nitrogen adsorption and desorption studies were performed to characterize the BP.

3.1.1 Raman Spectroscopy

[...on the same BP each](#)

Raman spectroscopy was performed on the Buckypaper for three different beams (532 nm, 633 nm, 785 nm), at three different spots (tests 1, 2 and 3) of the same BP each.

The raman shift of all tests was plotted as obtained (a)), and with the normalized values (b)) in Figures [3.3](#), [3.2](#) and [3.1](#). For tests 2 and 3, in the normalized graphs a 0.015 and 0.03 increase in all values of normalized intensity respectively was considered in order to have a better view of the graphs. For the same purpose, a displacement was also performed on the non-normalized graphs, a 500 and 1000 increase in counts for all of the values of tests 2 and 3 respectively.

Amount of material analyzed and concentration are important factors, the graphs were normalized to minimize the effect of the quantity analyzed and have a better comparison of concentrations in the tests.

The resulting graphs (Figures [3.3a](#), [3.2a](#) and [3.1a](#)) from evaluating three different spots of the same BP on the same beam are similar, which suggests a consistency on the amount of material analyzed, this happens for all 3 beams. After normalizing the graphs (Figures [3.3b](#), [3.2b](#) and [3.1b](#)), the similarity between graphs increases even more, suggesting that even in the spots were thickness was not exactly the same, the concentration was very similar.

For the 785 nm beam test (Figure [3.1](#)), which is the one commonly used for char-

acterization, the radial breathing mode shows only two main peaks at frequencies of 233.12 and 266.7 cm⁻¹ (Table 3.1). Using the parameters for A and B commonly used for SWCNT's ($A=234 \text{ nm/cm}$, $B=10 \text{ cm}^{-1}$) [41], **the diameter distribution of the carbon nanotubes on the Buckypaper ranges between 0.91 and 1.05 nm** by solving Equation 2.1:

$$w_{RBM} = A/d_t + B$$

$$\text{Thus, } dt = A/(w_{RBM} - B)$$

For the first peak:

$$dt = 234 \text{ nm/cm } / (233.12 \text{ cm}^{-1} - 10 \text{ cm}^{-1})$$

$$dt = 1.05 \text{ nm}$$

For the second peak:

$$dt = 234 \text{ nm/cm } / (266.7 \text{ cm}^{-1} - 10 \text{ cm}^{-1})$$

$$dt = 0.91 \text{ nm}$$

Also from Figure 3.1, the G band appears with a peak at 1592.38 cm⁻¹ with an intensity between 31672 (Test 1) and 33924 (Test 3) and the D band with peaks at 1292.21 (Test 1) and 1291.15 cm⁻¹ (Tests 2 and 3) with intensities between 1934.51 and 1985.68. Thus, the average G/D of 16.61 shows a low number of defects on the sample [5]. However, it's still considered as a medium quality CNT structure, since only a G/D > 20 is considered a high-quality CNT [13].

Table 3.1: Values where some raman features are found on Figure 3.1a.

Test	Band	Raman shift (cm ⁻¹)	Intensity (A.U.)
1	RBM peak 1	233.12	10655.14
2	RBM peak 1	233.12	11066.37
3	RBM peak 1	233.12	11552.89
1	RBM peak 2	266.7	8216.26
2	RBM peak 2	266.7	7998.77
3	RBM peak 2	266.7	8381.32
1	G	1592.38	31672.43
2	G	1592.38	32127.85
3	G	1592.38	33924.62
1	D	1292.21	1934.51
2	D	1291.15	1964.58
3	D	1291.15	1985.68

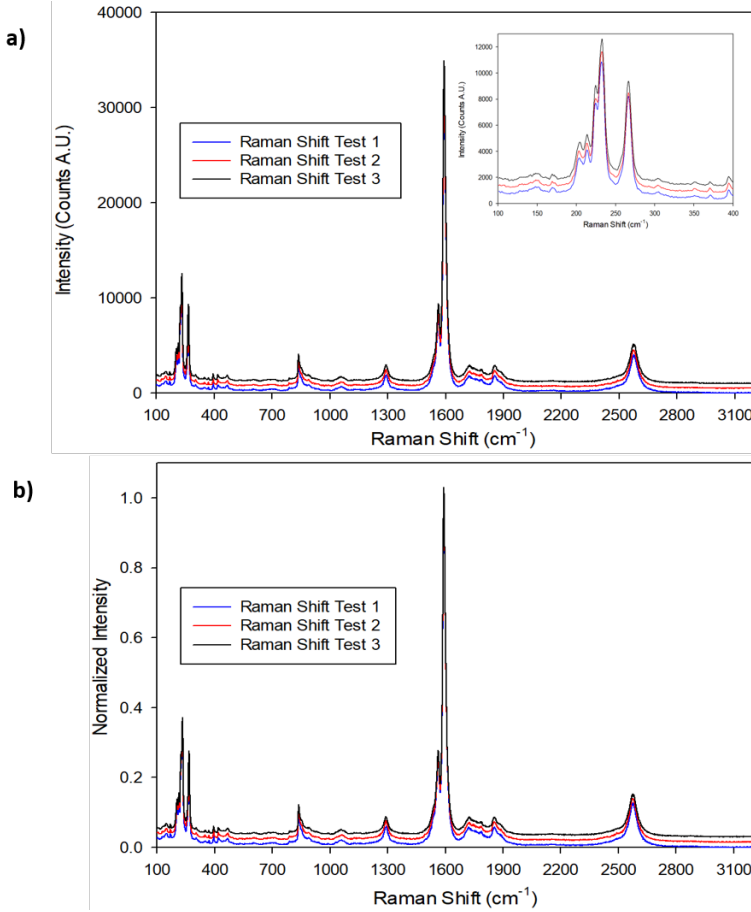


Figure 3.1: Raman spectroscopy at 785nm beam of a BP at three different spots, with a 500 counts displacement between each (a), and normalized graph with a .015 normalized intensity displacement each (b). RBM region zoomed in (a).

Table 3.2: Values where some raman features are found on Figure 3.2a.

Test	Band	Raman shift (cm^{-1})	Intensity (A.U.)
1	RBM highest peak	191.01	2134.78
2	RBM highest peak	191.01	2053.98
3	RBM highest peak	191.01	2067.24
1	RBM 2° highest peak	255	1651.88
2	RBM 2° highest peak	255	1629.98
3	RBM 2° highest peak	255	1674.99
1	G	1589.7	21703.16
2	G	1591.4	20249.95
3	G	1591.4	20820.80
1	D	1311.41	1098.70
2	D	1313.18	1052.49
3	D	1311.41	1073.35

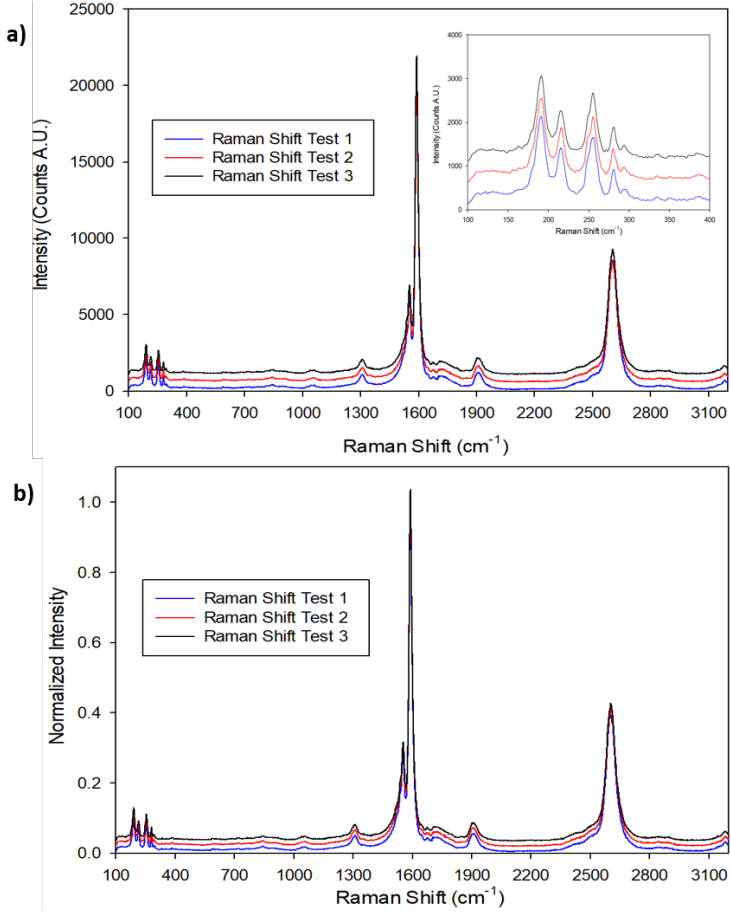


Figure 3.2: Raman spectroscopy at 633nm beam of a BP at three different spots, with a 500 counts displacement between each (a), and normalized graph with a .015 normalized intensity displacement each (b). RBM region zoomed in (a).

Table 3.3: Values where some raman features are found on Figure 3.3a.

Test	Band	Raman shift (cm^{-1})	Intensity (A.U.)
1	RBM peak 1	233.15	2471.78
2	RBM peak 1	233.15	2437.77
3	RBM peak 1	233.15	3213.31
1	RBM peak 2	269.40	3990
2	RBM peak 2	269.40	3865.23
3	RBM peak 2	267.49	4321.32
1	G	1589.97	22908.53
2	G	1589.97	22951.77
3	G	1589.97	26821.33
1	D	1328.19	3048.15
2	D	1329.86	3029.38
3	D	1329.86	3492.45

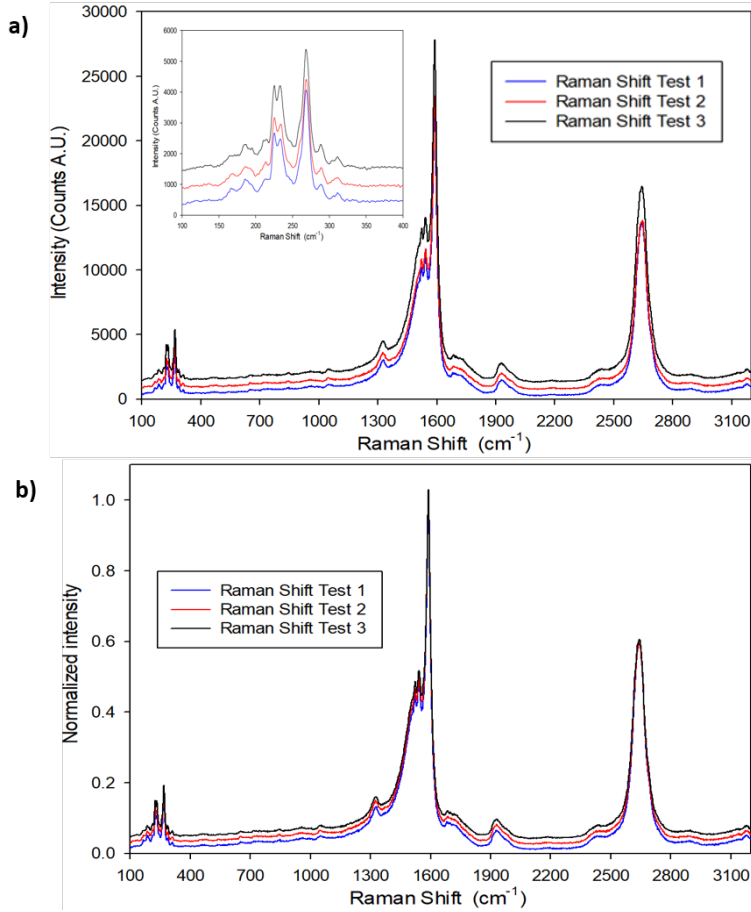


Figure 3.3: Raman spectroscopy at 532nm beam of a BP at three different spots, with a 500 counts displacement between each (a), and normalized graph with a .015 normalized intensity displacement each (b). RBM region zoomed in (a).

3.1.2 X-ray Photoelectron Spectroscopy

The three main elements found in the XPS were Carbon, Iron and Oxygen. This indicating that the SWCNTs do have some iron impurities (Figure 3.5) .

Table 3.4: Values for certain regions on Figure 3.5.

Region	Binding Energy (eV)	c/s (A.U.)
C1s	284.5	14325
C1s	285	10500
C1s	286	3712.5
O1S	530	3037.5

The C1s region peaks at a Binding Energy of 285 and 284.5 eV. C-C states appear close to the 284.8 eV values, while C-O-C interactions appear at 286 eV [1] . Since the

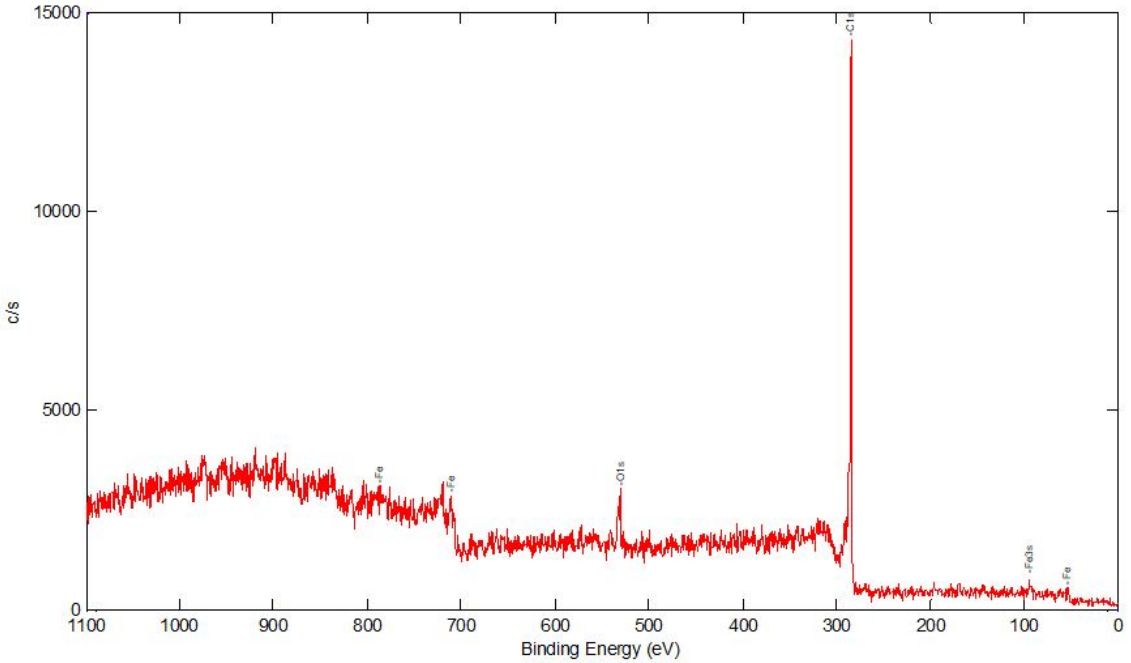


Figure 3.4: X-ray Photoelectron Spectroscopy of a BP.

carbon nanotubes were fabricated through the HiPCO method, which involves feeding carbon monoxide and a catalyst precursor into a furnace, with catalytic reactions occurring in the gas phase, some CNTs could have oxidized. Deconvolution of the C1s spectra analyzes the concentration of those C-O bonds, this technique was used in a study of Dodecylamine functionalization of CNT [8], it will be considered as future work to further characterize the material.

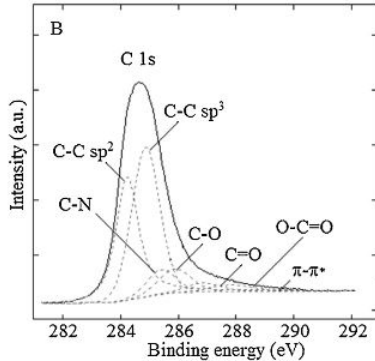


Figure 3.5: Visual representation of a C1s region deconvolution from XPS data. Extracted from [8].

The O1s region shows a peak at 530 Ev, which indicates the presence of metal oxides [2]. Since carbon pentacarbonyl is used as the precursor, it makes sense that metal oxide impurities are also detected, as it tells us that the SWCNTs are not highly purified.

No nitrogen was detected, indicating that the N,N-Dimethylformamide evaporated completely.

3.1.3 Nitrogen Physisorption

Three CNT films weighting in total 0.0788 g, were tested as a single sample to evaluate surface area and pore structure through the Brunauer-Emmett-Teller (BET), Density Functional Theory (DFT), and Barret-Joyner-Halenda (BJH) methods with the Quantachrome software.

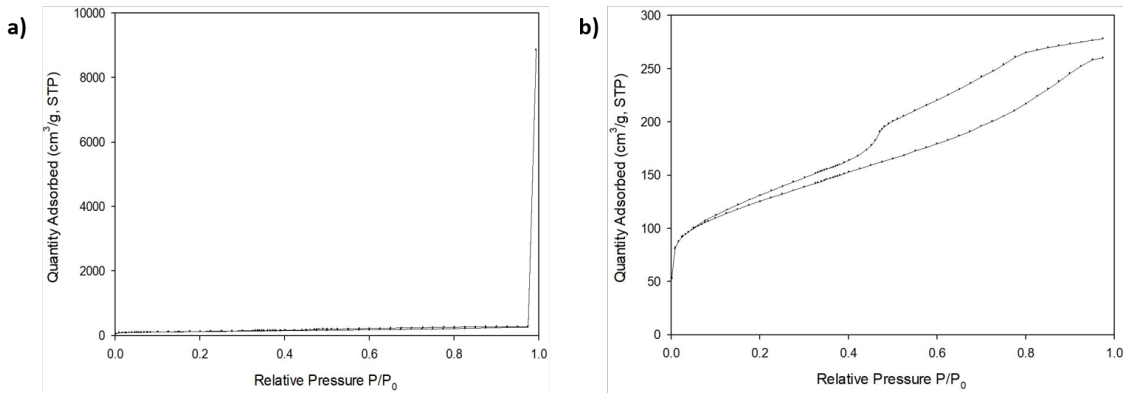


Figure 3.6: Isotherm graph for the adsorption (lower line) and desorption (higher line) of nitrogen with all the data (a), and removing the highest adsorption/desorption value (b).

The obtained isotherm (Figure 3.6) shows a Type IV(a) isotherm (Figure 2.7).

Type IV isotherms are characteristic of mesoporous (2-50 nm pore width) adsorbents with gas condensing in some pores at a smaller pressure than the saturation pressure of the bulk liquid [42][43]. In Type IV(a) isotherms, hysteresis also occurs when pore width exceeds a critical width that depends on the adsorption system. For nitrogen adsorption at 77 K, hysteresis starts to occur on pores wider than 4 nm [43][44].

Hysteresis loops have been classified into 6 different types (Figure 3.7) by the IUPAC [6], and they are related to particular features of the pore structure and adsorption mechanism. Since the end part of the obtained isotherm (Figure 3.6b) was cut when disregarding the last two values, the hysteresis presented has similarities to types H3, H4 and H5 (Figure 3.7), with the common characteristic on those three types being a desorption drop on the P/P_0 range of 0.4-0.5 for nitrogen at 77K [6]. For the BP it happens at 0.46 P/P_0 (Figure 3.6).

Type H3 loops have an adsorption branch similar to type II isotherms. They're usually given by non-rigid aggregates of plate-like particles like clays, and also if the pore network consists of macropores that aren't completely filled with pore condensate.

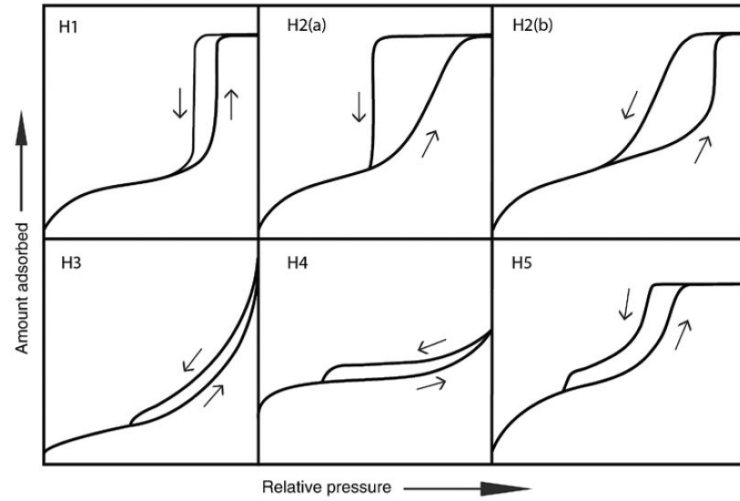


Figure 3.7: Classification of hysteresis loops. Extracted from [6].

Type H4 loops show an adsorption curve looking like a composite of isotherm types I and II, with a more pronounced adsorption than type H3 loops at low P/P_0 . This is associated to the filling of micropores and is often found on some mesoporous zeolites and micro-mesoporous carbons.

Type H5 loop appears for certain pore structures with both open and partially blocked mesopores.

Out of the three types, the H4 is the one more characteristic of carbon structures, which creates the expectation of a micro-mesoporous pore network from the DFT and BJH pore size distribution.

In the article "Liquid Infiltration into Carbon Nanotube Fibers:Effect on Structure and Electrical Properties" [9], J. Qiu also performed the nitrogen adsorption-desorption method on MWCNT fiber (Figure 3.8).

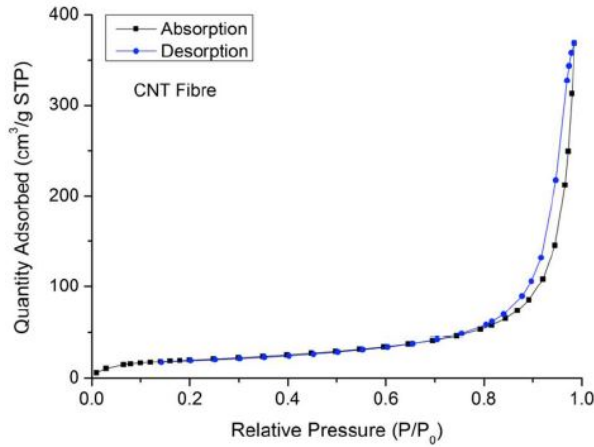


Figure 3.8: Isotherm plot for the CNT fibers. Retrieved from [9].

The MWCNT fiber adsorbed and desorbed no more than 400 (cm^3/g STP) at a relative pressure close to 1, while in Figure 3.6 there is an abrupt increase in the quantity adsorbed/desorbed from 260 (cm^3/g STP) to 8800 (cm^3/g STP). It is important to note that the BP had to be cut in smaller pieces to fit on the test vials, bigger pores could have been formed when cutting, leading to that abrupt increase. For comparison reasons, the DFT and BJH theory will be applied with and without the last adsorption and desorption values (Figure 3.6b).

BET surface area

BET surface area was calculated as explained in chapter 2, with the help of the Quantachrome software.

From the data range selected by the software from the isotherm, which corresponded to the values of p/p^0 from 0.0748 to 0.1743, the BET plot (Figure 3.9) was built with values from Table 3.5, where g_{BP} are grams of BP and g_{N_2} grams of Nitrogen gas absorbed.

Table 3.5: BET plot data points.

p/p^0	$\frac{1}{W(p^0/p-1)} (g_{BP}/g_{N_2})$
7.477×10^{-2}	6.149×10^{-1}
7.551×10^{-2}	6.198×10^{-1}
8.219×10^{-2}	6.718×10^{-1}
9.901×10^{-2}	8.001×10^{-1}
1.243×10^{-1}	9.959×10^{-1}
1.496×10^{-1}	1.194
1.743×10^{-1}	1.388

Using Equations 2.3 and 2.4, W_m and the C parameter are calculated:

$$W_m = \frac{1}{7.757 + 0.0338} (1 / \frac{g_{BP}}{g_{N_2}})$$

$$W_m = 0.1284 \frac{g_{N_2}}{g_{BP}}$$

$$C = 1 + \frac{7.757}{0.0338} (\frac{g_{BP}/g_{N_2}}{g_{BP}/g_{N_2}})$$

$$C = 230.5$$

Values of C higher than 150 are generally associated with filling of narrow micropores, which is in accord with the DFT pore distribution (Figure 3.11)

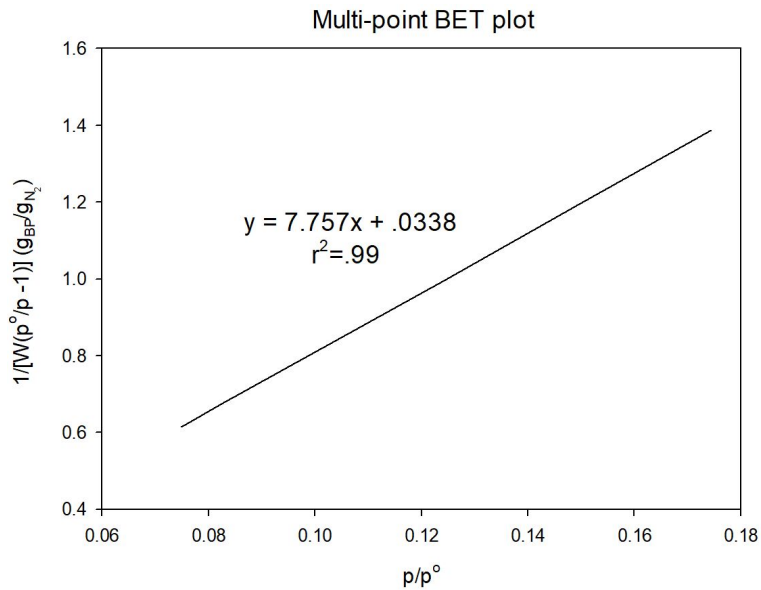


Figure 3.9: BET plot generated from the BP physisorption isotherm and its equation (linear regression).

BET surface area is now calculated with Equation 2.5:

$$A_s = 0.1284 \frac{g_{N_2}}{g_{BP}} * \frac{1}{28} \frac{\text{mol}_{N_2}}{g_{N_2}} * 6.022 \times 10^{23} \frac{\text{molecules}_{N_2}}{\text{mol}_{N_2}} * 1.62 \times 10^{-19} * \frac{m^2}{\text{molecules}_{N_2}}$$

$$A_s = 447.21 \frac{m^2}{g_{BP}}$$

Which is very close to the $447.01 \frac{m^2}{g_{BP}}$ obtained with the software.

Non-Local Density Functional Theory pore analysis:

The NLDFT was used to obtain the Pore System Distribution (PSD)

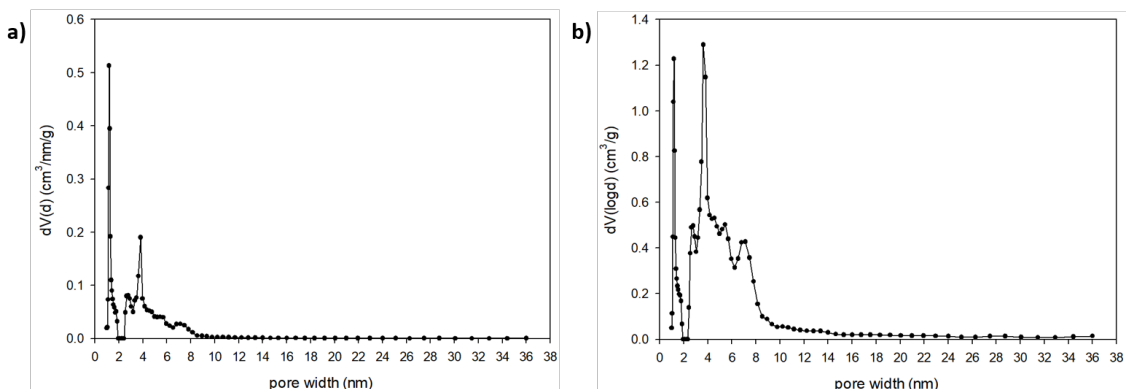


Figure 3.10: The cumulative volume that pores of the same width amount to per nm (a) and it's total volume contribution per gram of BP (b) by the DFT.

The pore that appears the most on the BP has an average width of 1.178 nm (Figure 3.10a). However the pores that contribute the most to the total pore volume have an

average width of 3.47 nm (Figure 3.10b). In general, nanopores, and mesopores of up to 8 nm constitute most of the porous system on the BP.

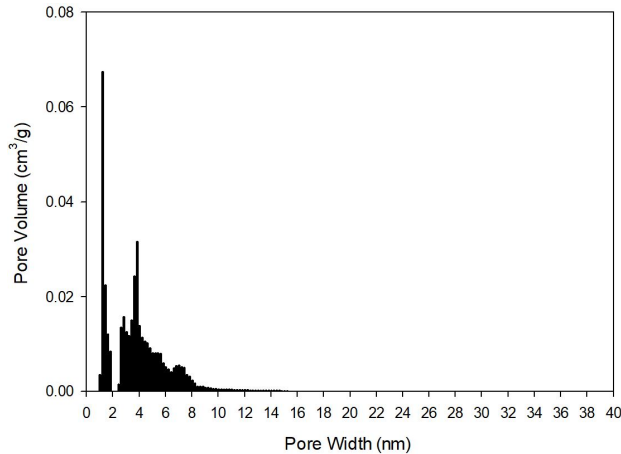


Figure 3.11: Distribution of the total pore volume by the total pore volume of all different pore widths by the DFT in a histogram, starting from a width of 1.05 nm and grouping every 0.2 nm increase.

By adding the total pore volume each individual pore width contributes to the total pore volume, the cumulative pore volume graph is formed (Figure 3.12).

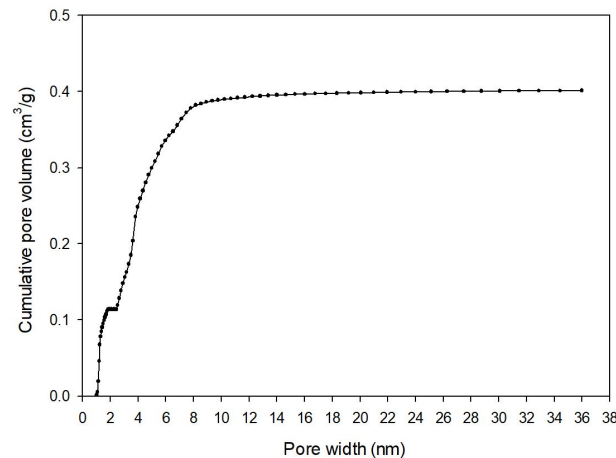


Figure 3.12: The cumulative pore volume formed by adding the total pore volume of all pore widths by the DFT.

The total pore volume results in **0.401 cm³/g_{BP}**.

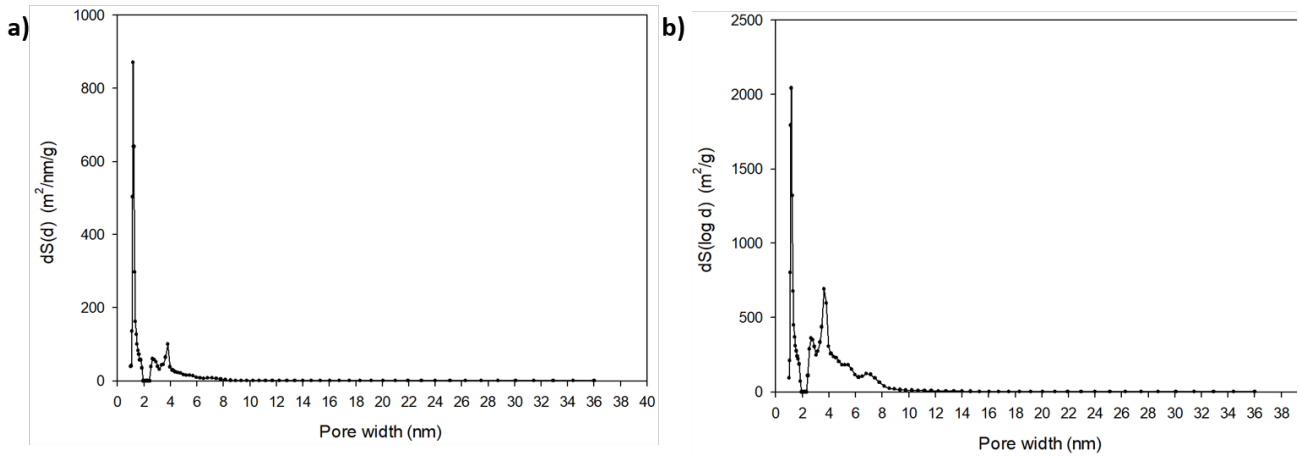


Figure 3.13: The cumulative surface area that pores of the same width amount to per nm (a) and it's total surface area contribution per gram of BP (b) by the DFT.

By adding the total surface area each individual pore width contributes to the total surface area, the cumulative surface area graph is formed (Figure 3.14).

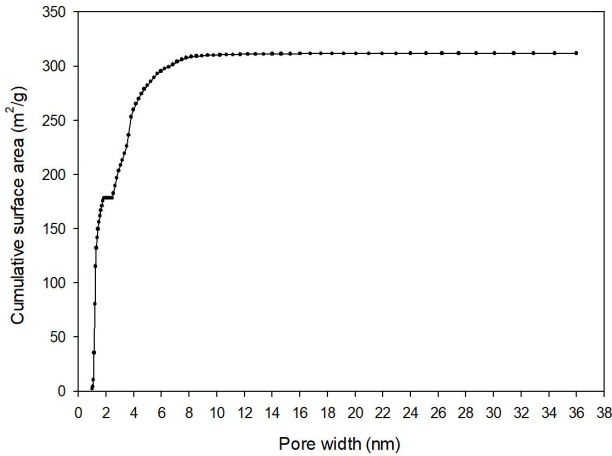


Figure 3.14: The cumulative surface area by the DFT.

The total surface area results in **311.82 m²/g**.

When using the DFT considering only values from Figure 3.6b, the surface area and pore volume remained the same since it doesn't use the full curve.

The BJH Theory:

Through applying this method, macropores with widths of 185.1 nm and 294.8 nm are detected when using values from Figure 3.6a, while only maximum widths of 58.59 nm are found when considering values from Figure 3.6b (Figure 3.15). In both cases no nanopores of widths lower than 2 nm are observed. The fact that the PTFE filter used to filter the CNT's has a pore average width of 450 nm could be important when explaining why there were those macropores.

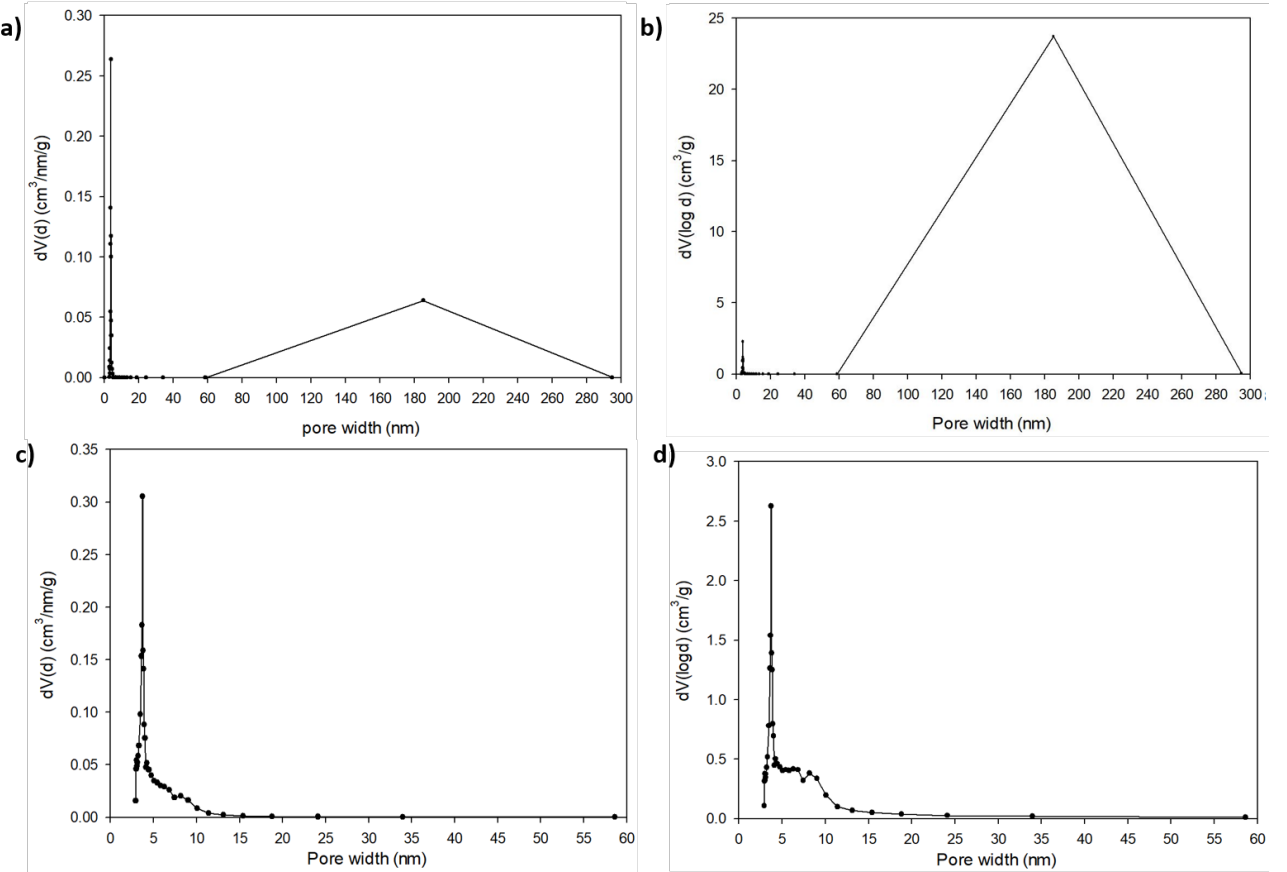


Figure 3.15: The cumulative volume that pores of the same width amount to per nm using all isotherm desorption values(a) and it's total volume contribution per gram of BP (b). The cumulative volume that pores of the same width amount to per nm omitting the highest desorption value (c) and it's total volume contribution per gram of BP (d), all obtained with the BJH method.

Both using the full desorption curve and omitting the highest value, the pore that appears the most on the BP has an average width of 3.736 nm (Figure 3.15a and c). However, in the first case the 185.1 nm pores contribute the most to the total pore volume (Figure 3.15a).

By adding the total pore volume each individual pore width contributes to the total pore volume, the cumulative pore volume graph is formed (Figure 3.16).

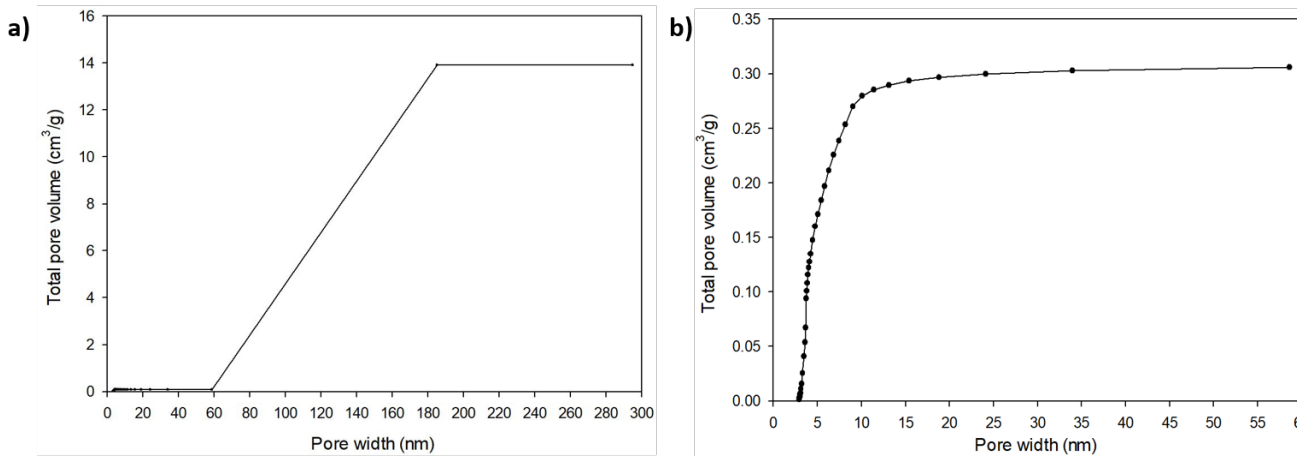


Figure 3.16: The cumulative pore volume formed by adding the total pore volume of all pore widths calculated by the BJH theory using all desorption values (a) and omitting the highest desorption value (b) by the BJH method.

The total pore volumes result in **13.915 $\text{cm}^3/\text{g}_{BP}$** (Figure 3.16a) and **0.306 $\text{cm}^3/\text{g}_{BP}$** (Figure 3.16b). This is expected since not considering the higher desorption value means disregarding the bigger pores detected in Figure 3.15a.

By adding the total surface area each individual pore width contributes to the total surface area (Figure 3.18), the cumulative surface area graph is formed (Figure 3.17).

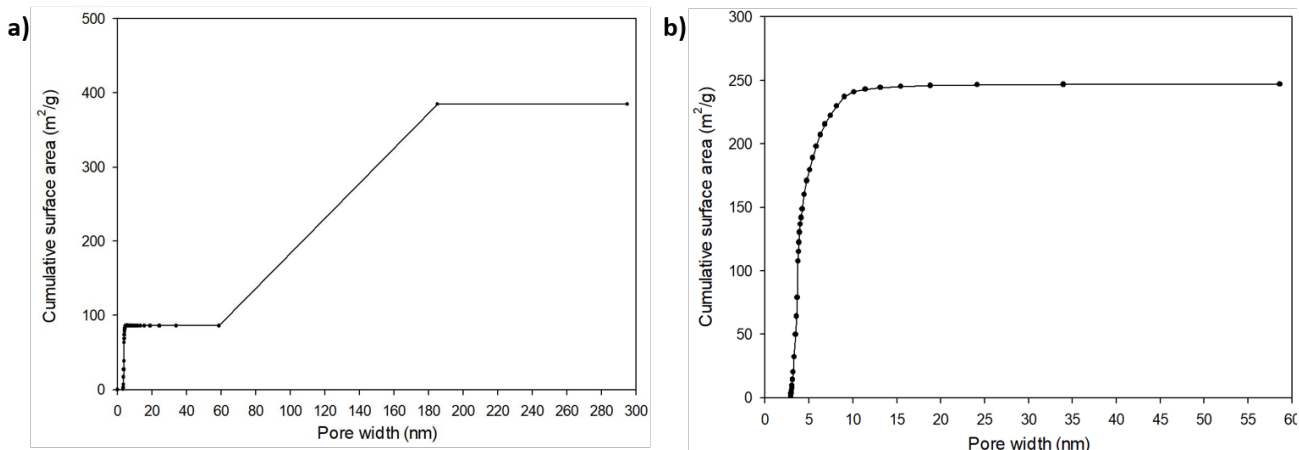


Figure 3.17: The cumulative surface area when using all desorption values (a) and when omitting the highest desorption value, both obtained through the BJH theory.

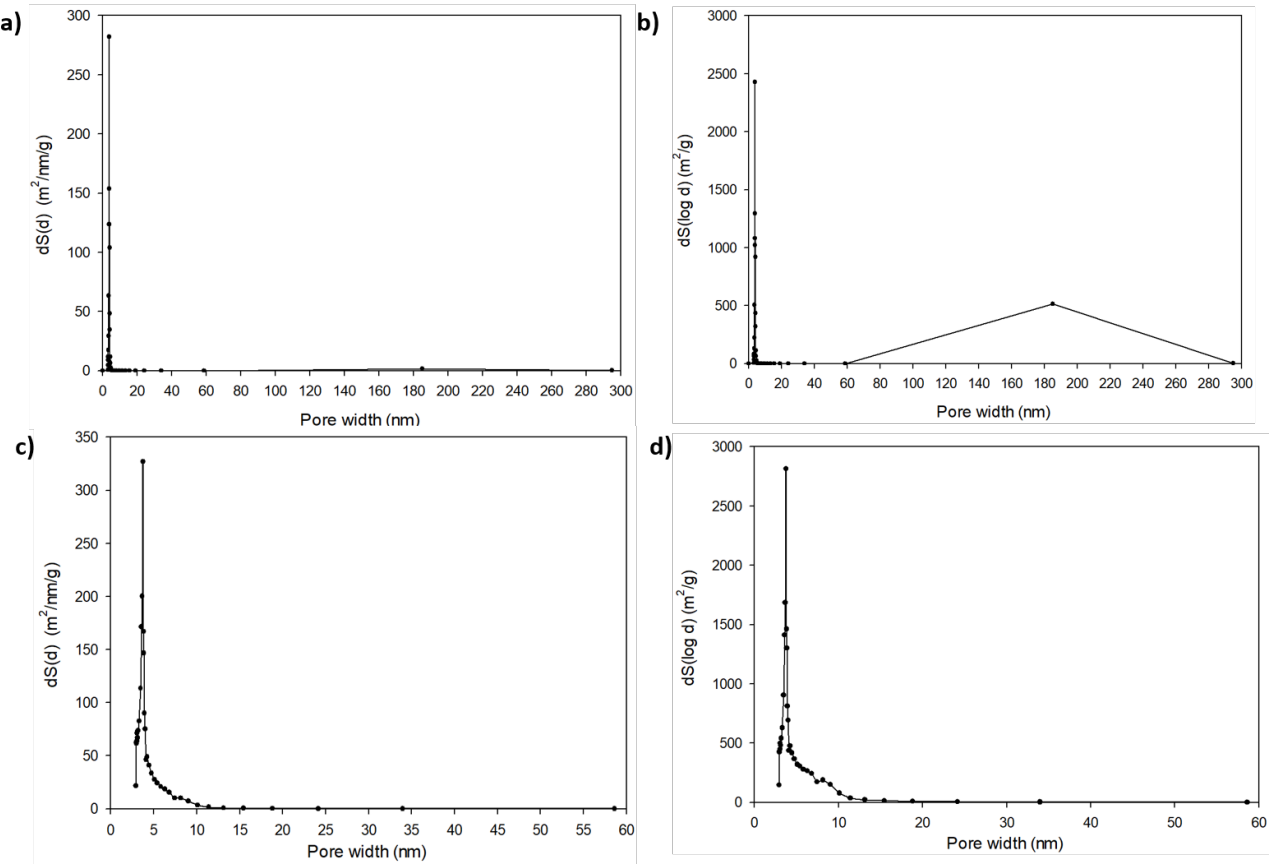


Figure 3.18: The cumulative surface area that pores of the same width amount to per nm using all isotherm desorption values(a) and it's total surface area contribution per gram of BP (b). The cumulative surface area that pores of the same width amount to per nm omitting the highest desorption value(c) and it's total surface area contribution per gram of BP (d), all obtained with the BJH theory.

The total surface areas result in **384.98 m²/g** (Figure 3.17a) and **246.99 m²/g**.

Values obtained from DFT,BHJ theory and BET analysis are shown in Table 3.6.

Table 3.6: Data obtained from physisorption results (pore width is the pore with the highest mode).

Method	Surface Area (m ² /g _{BP})	Pore Volume (cm ³ /g _{BP})	Pore width (nm)
BET	447.010	-	-
DFT	311.82	0.401	1.178
BJH	384.98	13.915	3.736
BJH*	246.99	0.306	3.736

BJH* represents the values obtained omitting the highest desorption value from the isotherm.

The DFT is more efficient when analyzing mesoporous structures than the BJH theory, but since the methodology uses a template that doesn't consider bigger pores, consideration of both methods is important.

To calculate porosity, the dimensions of the BP are measured. The thickness of the BP was observed using images from a Scanning Electron Microscope at a 1349 x magnification, at 4 different spots of a 0.0254 g BP (Figure 3.19). From the images, thickness was measured on 5 different spots each, with the average resulting in 34.0825 μm (Table 3.7).

Table 3.7: Thickness measurements on 20 different spots of a BP.

Measurement	Thickness (μm)
1	30.48
2	33.71
3	33.49
4	35.2
5	31.31
6	35.85
7	36.93
8	36.5
9	37.17
10	37.58
11	37.16
12	38.88
13	36.78
14	37.39
15	27.86
16	33.04
17	33.91
18	33.56
19	26.56
20	28.29
Average	34.0825

For the diameter a Vernier was used. Since it's filter setup dependant, only one sample was measured, obtaining a diameter of 35.4 mm.

Since the BP has a cylindrical geometry, area was calculated as a circle and then multiplied by the thickness.

$$A = \pi(3.54 \text{ cm})^2 / 4 = 9.8423 \text{ cm}^2$$

$$V = 9.8423 \text{ cm}^2 * 0.0034 \text{ cm} = 0.0335 \text{ cm}^3$$

Total volume is 0.0335 cm^3 , thus density is 0.7582 g/cm^3 .

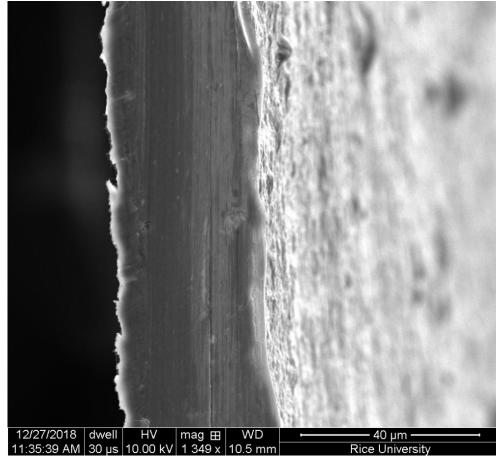


Figure 3.19: Side view of a BP at a 1349x magnification with a SEM.

With the weight of the BP used, porous volume and porosity was calculated from the DFT and BJH results (Table 3.6). The total pore volume is first obtained, and then divided by the total volume to get porosity.

$$\text{DFT Total pore volume} = 0.401 \text{ cm}^3/\text{g} * 0.0254 \text{ g} = 0.0102 \text{ cm}^3$$

$$\text{BJH Total pore volume} = 13.915 \text{ cm}^3/\text{g} * 0.0254 \text{ g} = 0.3534 \text{ cm}^3$$

$$\text{BJH* Total pore volume} = 0.306 \text{ cm}^3/\text{g} * 0.0254 \text{ g} = 0.0078 \text{ cm}^3$$

$$\text{DFT Porosity} = 0.0102 \text{ cm}^3 / 0.0335 \text{ cm}^3 * 100 = \mathbf{30.448\%}$$

$$\text{BJH Porosity} = 0.3534 \text{ cm}^3 / 0.0335 \text{ cm}^3 * 100 = \mathbf{1054.925\%}$$

$$\text{BJH* Porosity} = 0.0078 \text{ cm}^3 / 0.0335 \text{ cm}^3 * 100 = \mathbf{23.284\%}$$

Table 3.8: Porosity calculation of the BP from the DFT and BJH results.

Method	Pore Volume ($\text{cm}^3/\text{g}_{BP}$)	Total Pore Volume (cm^3)	Porosity (%)
DFT	0.401	0.0102	30.448
BJH	13.915	0.3534	1054.925
BJH*	0.306	0.0078	23.284

Porosity was also calculated by a different method, as shown in the study from L. Zhang et al. [25] (except that density of the BP is used instead of density of a fiber), where they use Equation 3.1 and obtained a 23.7% porosity on their multi-walled carbon nanotube (MWCNT) fiber.

$$P = 1 - \rho_{fiber}/\rho_{CNT} \quad (3.1)$$

Commercial SWCNTs from Sigma Aldrich (98% semiconducting, 98% metallic, <1% metal catalyst and <3.5% metal catalyst) have a reported density range of 1.7-1.9 g/cm³ at 25°C. While Q. Lu reported density for isolated acid-treated and untreated SWCNTs at room temperature by the gradient sedimentation as 1.74 g/cm³ and 2.13 g/cm³ respectively [21].

Table 3.9: (Theoretical porosity calculation of the BP using reported SWCNT densities.

SWCNT Density (g/cm ³)	Porosity (%)
1.7	55.400
1.74	56.425
1.9	60.095
2.13	64.404

In [9], MWCNT fiber was reported with a 54.4% porosity through the BHJ method results for pore volume, and a surface area of $75.6 \pm 0.7 (\text{m}^2/\text{g})$ through the BET method. That porosity is more similar to those obtained with the theoretical SWCNT values (Table 3.9). However, the surface area obtained with BET is over the 400 m²/g, which falls into what commercial 90% pure SWCNTs from NanoArmor report (>380 m²/g) [45].

There are 3 main types of pores:

The pores inside the SWCNT diameter.

The pores formed between SWCNTs.

The pores formed between bundles of SWCNTs.

For the pores inside the SWCNT diameter, an approximation of considering a BP with a mass of 0.0254 g as an infinitely long cylinder (Figure 3.20) with an average diameter of 0.98 nm (obtained from the raman section), wall thickness and density allows for an estimation to be calculated.

An approximate CNT wall thickness of 0.101 nm was estimated in [10] for a SWCNT of a 0.982 nm diameter, a (10,5) chirality and an aspect ratio of 5.29. This value was chosen based only from diameter similarity since chirality and aspect ratio is not known.

An average density of 1.8 g/cm³ for semiconducting SWCNTs from Sigma-Aldrich [19] is used.

Not taking into consideration the weight of air inside the SWCNTs:

$$\text{Total volume} = 0.0254 \text{ g} / 1.8 \frac{\text{g}}{\text{cm}^3} = 0.0141 \text{ cm}^3$$

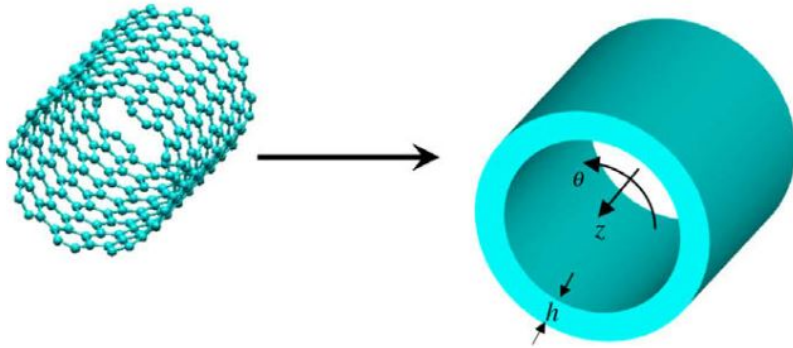


Figure 3.20: Representation of a SWCNT as a cylinder. Extracted from [10].

$$\text{Cylinder volume} = \frac{\pi * d^2 * L}{4}$$

$$\text{Length}(L) = \frac{4 * 0.0141\text{cm}^3}{\pi * (9.82 * 10^{-8}\text{cm})^2} = 1.82 * 10^{12} \text{ cm}$$

$$\text{Inner volume} = \frac{\pi * (9.82 * 10^{-8}\text{cm} - 1.01 * 10^{-8}\text{cm})^2 * 1.82 * 10^{12}\text{cm}}{4}$$

$$\text{Inner volume} = \mathbf{0.0111 \text{ cm}^3}$$

This inner volume doesn't consider the holes produced in the wall, only the inner diameter.

Considering a total pore volume of 0.0102 cm^3 resulting from the DFT porosity data could mean that the actual porosity is higher and N_2 is not entering the inner diameter on all the SWCNTs (it can enter since a N_2 molecule has an effective diameter of 0.3 nm, while the average inner diameter of the SWCNT is around 0.88 nm). However, ends of SWCNT's are originally closed, and the % of CNT's with open ends is unknown.

3.1.4 Wettability

In this section, the wettability between the coating and the BP is analyzed.

When measuring contact angles for porous surfaces, a dynamic contact angle measurement is preferred, since fast penetration of a measuring liquid into the porous structure could difficult the measurement of a static angle. Also, for granulated and powder materials, a drop cannot be placed because of geometrical reasons relating to these materials. As for thin fibres, only small drops can be placed, which also requires specialized dosing and measuring devices, which could result in large errors.

The Wilhelmy Plate method is the main way to calculate dynamic contact angles.

However, a tensiometer is required for inserting the solid on the liquid and such an equipment was not available. As for the Washburn theorem [46] for contact angles on porous surfaces, a tensiometer and software able to track mass adsorption on the surface is also needed. That's why, although it's not the optimal way, after forming droplets through the sessile drop method (Figure 3.21), the initial contact angle of liquids on the BP was measured and used for calculation.

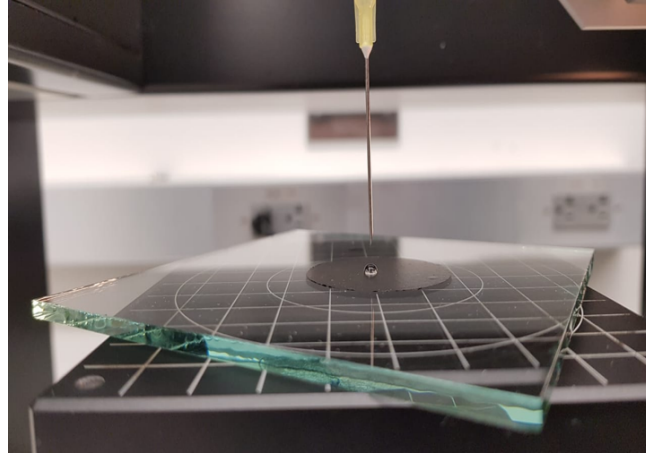


Figure 3.21: Droplet of water on top of a BP.

Buckypaper surface

Surface of the BP was observed from SEM images (Figure 3.22b) and compared to the surface of a MWCNT fiber (Figure 3.22a).

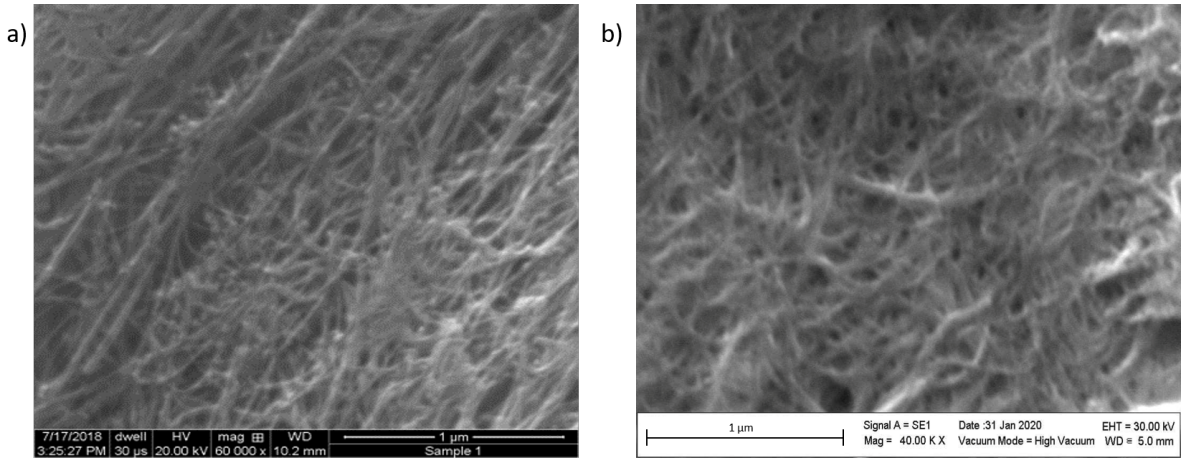


Figure 3.22: MWCNT fiber surface taken at Rice University by Dr. Lucas at a 60,000x magnitude and 10.2 mm working distance (WD) (a) and surface of a SWCNT buckypaper taken at ITESM at a x40,000 magnitude and 5 mm WD (b).

The fiber surface has more alignment due to the direction given when forming it. However, their structures look very similar. Henceforth, it's one of the reasons that

BP is used in this investigation as an approximation to CNT fibers, they are also easier to make at a laboratory scale.

Using Image J as measurement software, in scale, $1 \mu\text{m}$ from Figure 3.22b is $0.9 \mu\text{m}$ from Figure 3.22a.

From Figure 3.22, porosity could be interpreted as the open holes formed between bundles of CNTs, suggesting that a Wenzel [36], Cassie-Baxter [37], or an intermediate state will take place.

Surface free energy (γ_{SV})

There are many different theories for converting contact angle data into solid surface energy values. The most used one is the Owens-Wendt theory [47].

Owens and Wendt divided the surface energy of a solid in two components. The dispersive component accounts for van der Waals and other non-site specific interactions between the liquid and the solid, while the polar component considers dipole-dipole, dipole-induced dipole, hydrogen bonding, and other site-specific interactions. The theory is based on two fundamental equation that describe interactions between solids and liquids, which are Young's equation (Equation 2.11) and Good's equation [48] (Equation 3.2), which relates to the energy difference for the liquid molecule to reside on the surface.

$$\gamma_{LS} = \gamma_S + \gamma_L - 2(\gamma_L^D \gamma_S^D)^{1/2} - 2(\gamma_L^P \gamma_S^P)^{1/2} \quad (3.2)$$

Where:

γ_L = Overall surface tension of the wetting liquid.

γ_L^D = Dispersive component of the surface tension of the wetting liquid.

γ_L^P = Polar component of the surface tension of the wetting liquid.

γ_S = Overall surface energy of the solid.

γ_S^D = Dispersive component of the surface energy of the solid.

γ_S^P = Polar component of the surface energy of the solid.

γ_{LS} = Interfacial tension between the solid and the liquid.

θ = Contact angle between the liquid and the solid.

Combining both equations results in Equation 3.3.

$$\frac{\gamma_L(\cos\theta + 1)}{2(\gamma_L^D)^{1/2}} = (\gamma_S^P)^{1/2} \frac{(\gamma_L^P)^{1/2}}{(\gamma_L^D)^{1/2}} + (\gamma_S^D)^{1/2} \quad (3.3)$$

This equation has the form $y = mx + b$ from which:

$$y = \frac{\gamma_L(\cos\theta + 1)}{2(\gamma_L^D)^{1/2}}$$

$$m = (\gamma_S^P)^{1/2}$$

$$x = \frac{(\gamma_L^P)^{1/2}}{(\gamma_L^D)^{1/2}}$$

$$b = (\gamma_S^D)^{1/2}$$

Regardless of this method only requiring a minimum of two testing liquids, for a more precise measurement three liquids were chosen (water, diiodomethane and glycerol).

The polar, and disperse components of the liquids can be looked for in the literature (Table 3.10).

Table 3.10: Polar and dispersive surface energy components of the test liquids. Extracted from [4].

Liquid	γ_L (mJ/m ²)	γ_L^P (mJ/m ²)	γ_L^D (mJ/m ²)
Water	72.8	51.0	21.8
Diiodomethane	50.8	0.0	50.8
Glycerol	64.0	30.0	34.0

Three droplets of each liquid were measured on three different Buckypapers, and the values were averaged (Table 3.11).

Table 3.11: Contact Angle (CA) values for High Performance Liquid Chromatography (HPLC) grade water, glycerol and diiodomethane droplets on BP.

Sample/drop	HPLC Water CA (°)	Glycerol CA (°)	Diiodomethane CA (°)
S1D1	45.45	32.11	17.64
S1D2	45.07	44.8	14.49
S1D3	46.12	35.08	19.02
S1 Avg	45.55	37.33	17.05
S2D1	48.38	38.84	18.77
S2D2	48.93	34.38	16.59
S2D3	52.71	40.64	18.44
S2 Avg	50.01	37.95	17.93
S3D1	51.86	44.09	20.3
S3D2	55.57	41.45	19.94
S3D3	49.6	42.68	20.72
S3 Avg	52.34	39.32	20.32
Total Avg	49.30	39.32	18.43

From the total averages, the y and x were calculated for the three liquids.

Water:

$$\frac{\gamma_L(\cos\theta + 1)}{2(\gamma_L^D)^{1/2}} = \frac{72.8mJ/m_2(\cos49.3 + 1)}{2(21.8mJ/m_2)^{1/2}} = 12.8798 \text{ (mJ/m}_2\text{)}^{1/2}$$

$$\frac{(\gamma_L^P)^{1/2}}{(\gamma_L^D)^{1/2}} = \frac{(51mJ/m_2)^{1/2}}{(21.8mJ/m_2)^{1/2}} = 1.5295$$

Glycerol:

$$\frac{\gamma_L(\cos\theta + 1)}{2(\gamma_L^D)^{1/2}} = \frac{64mJ/m_2(\cos39.32 + 1)}{2(34mJ/m_2)^{1/2}} = 9.7335 \text{ (mJ/m}_2\text{)}^{1/2}$$

$$\frac{(\gamma_L^P)^{1/2}}{(\gamma_L^D)^{1/2}} = \frac{(30mJ/m_2)^{1/2}}{(34mJ/m_2)^{1/2}} = 0.9393$$

Diiodomethane:

$$\frac{\gamma_L(\cos\theta + 1)}{2(\gamma_L^D)^{1/2}} = \frac{50.8mJ/m_2(\cos18.43 + 1)}{2(50.8mJ/m_2)^{1/2}} = 6.9446 \text{ (mJ/m}_2\text{)}^{1/2}$$

$$\frac{(\gamma_L^P)^{1/2}}{(\gamma_L^D)^{1/2}} = \frac{(0mJ/m_2)^{1/2}}{(50.8mJ/m_2)^{1/2}} = 0$$

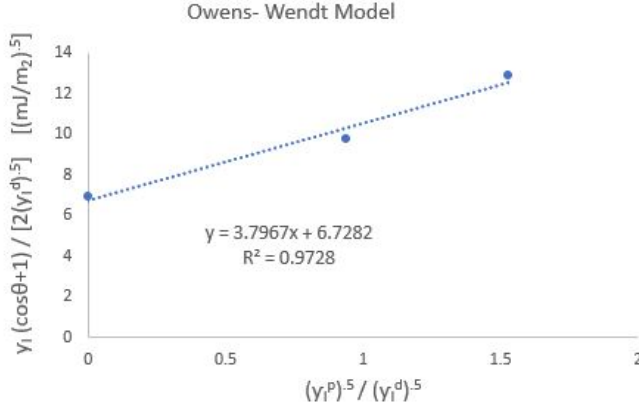


Figure 3.23: Graph obtained to calculate Owens-Wendt model parameters.

From the regression (Figure 3.23) we can calculate the surface free energy of the BP.

$$b = (\gamma_S^D)^{1/2} = 6.7282 \text{ (mJ/m}_2\text{)}^{1/2}$$

$$\gamma_S^D = (6.7282 \text{ (mJ/m}_2\text{)}^{1/2})^2 = 45.2687 \text{ mJ/m}_2$$

$$m = (\gamma_S^P)^{1/2} = 3.7967 \text{ (mJ/m}_2\text{)}^{1/2}$$

$$\gamma_S^P = (3.7967 \text{ (mJ/m}_2\text{)}^{1/2})^2 = 14.4149 \text{ mJ/m}_2$$

$$\gamma_S = \gamma_S^D + \gamma_S^P$$

$$\gamma_S = 45.2687 \text{ mJ/m}_2 + 14.4149 \text{ mJ/m}_2$$

$$\gamma_S = \mathbf{59.63 \text{ mJ/m}_2}$$

This value agrees with a theoretical estimation of 40-80 mJ/m₂ for the critical surface energy of single-walled CNTs [49].

By measuring the dynamic CA on MWCNT fiber, using the equilibrium CA and the acid-base theorem, in a study [25] a γ_S of 36.81 mJ/m₂ was obtained. The advancing and receding CA of water they obtained were $136^\circ \pm 6.7$ and $46.3^\circ \pm 8.6$ respectively.

Since a hydrophobic behavior of water on BP was expected, more contact angles were measured and few contact angles above 90° were obtained in the same BP, where mostly contact angles in the range of 45° - 55° were obtained (Figure 3.24).

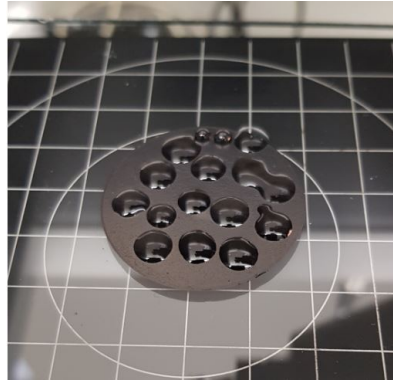


Figure 3.24: A BP with single drops of water applied through most of the surface.

The hydrophobic contact angle was observed for 40 minutes after being formed. By minute 35 when the contact angle was $\approx 20^\circ$ the software could no longer read the angle, and by minute 40 the drop was no longer visible on the surface.

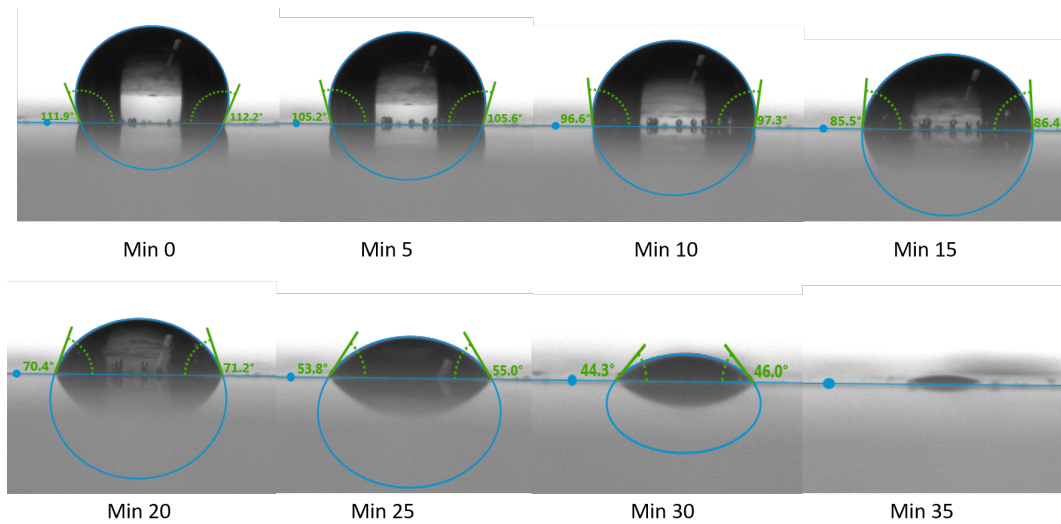


Figure 3.25: A drop of water on the surface of a BP, with contact angle measured for 35 minutes.

The Image J software was used on Figure 3.24 to measure the diameter projected on a drop of CA above 90° , with the drop of higher visible contact angle resulting in 0.251 cm diameter. Using minute 0 of Figure 3.25, the rest of the measurements were taken to calculate initial volume of the water drop (Figure 3.26).

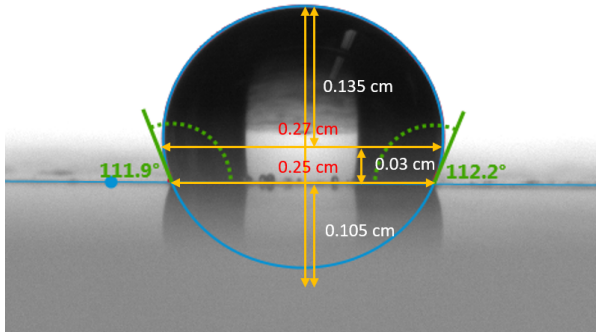


Figure 3.26: Measurements on a drop of water on top of a BP.

Considering an spherical drop of $r=0.27$ cm leads to a total volume of 0.0825 cm^3 .

Spherical volume:

$$V = \frac{4}{3} \pi r^3$$

$$V = \frac{4}{3} \pi (0.135 \text{ cm})^3$$

$$V = 0.0103 \text{ cm}^3$$

For the missing part, an ellipsoid of dimensions a, b and c ($r_1= 0.125$, $r_2= 0.125$ and height = 0.105 cm respectively) was considered, with volume divided by half.

Total ellipsoid volume:

$$V = \frac{4}{3} \pi abc$$

$$V = \frac{4}{3} \pi (0.125 \text{ cm})(0.125 \text{ cm})(0.105 \text{ cm})$$

$$V = 0.0069 \text{ cm}^3$$

Subtracting the half ellipsoid to the total volume of the sphere, results in a water drop volume of **0.0068 cm³**.

Water drop volume:

$$V = 0.0103 \text{ cm}^3 - 0.0035 \text{ cm}^3$$

$$V = 0.0068 \text{ cm}^3$$

The total pore volume of the BP considering DFT is 0.0102 cm^3 (Table 3.8). Thus, the drop can occupy the pore volume of the BP because of gravity and capillarity, regardless of it's hydrophobicity.

The first assumption for obtaining contact angles below and above 90° was that the N,N-Dimethylformamide was not completely evaporated, since the boiling point is 153°C and the BP was only heated at 80°C. However, the N,N-Dimethylformamide didn't show on the XPS (no nitrogen detected). Regardless, new BP were heated to 160°C and contact angles were measured and the same variation was obtained.

From the pore distribution (Figure 3.11), another possibility is that the spots on the BP where the lower CA were obtained where the ones with the bigger pores, thus a Wenzel behavior could have taken place and the apparent CA measured was below 90°, and when the spot had mostly the smaller pores, a CA higher than 90° was measured.

Presence of oxygen in the surface could also be a factor, since the surface would have more affinity to water, with a deeper analysis of the XPS, the C-O bonds can be identified.

A surface free energy study on graphene layers grown on copper [4], through the Owens-Wendt method obtained a γ_S of 53 mJ/m₂, and showed how over the course of 24 hours it decreased to 37.5 mJ/m₂ due to ambient conditions, as all of the contact angles for the testing liquids increased (Figure 3.27). Thus, humidity could be another cause of obtaining different contact angles.

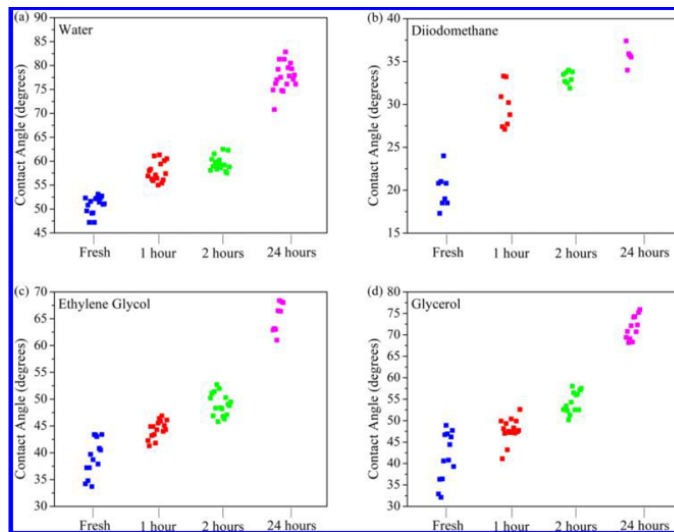


Figure 3.27: Change in contact angle on a graphene layer. Extracted from [4].

Coating surface tension

Surface tension of the coatings on the liquid-air interface was measured (Table 3.12). The only exception was the Epolene® wax, since it instantly cured at room temperature, and maintaining high temperatures on the syringe while on the KRÜSS DSA100S equipment proved to be a challenge.

Table 3.12: Surface tension of the coating-air interface.

Coating	Surface Tension (mN/m)
Glyptal® 1202 Insulating Varnish	29.75
Glyptal® 1201 Red Enamel	36.39
635 Thin Epoxy Resin with hardener	34.47

The measurements were taken with a very bright background illumination. However, a technical report from Krüss [50] suggests to use a gray illumination, since a bright background usually results in a narrower measurement of the drop that it actually is, and that can be seen as a red curvature indicator on Figure 3.28, 3.29 and 3.30.



Figure 3.28: Measurement of surface tension on the red enamel-air interface through the pendant drop method.

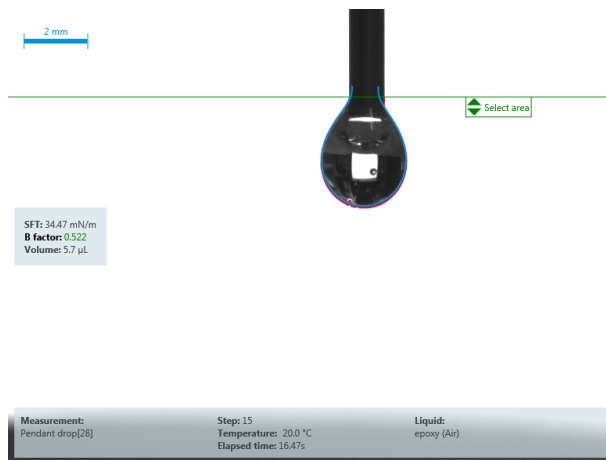


Figure 3.29: Measurement of surface tension on the epoxy-air interface through the pendant drop method.



Figure 3.30: Measurement of surface tension on the insulating varnish-air interface through the pendant drop method.

CA of coatings on BP

At room temperature, initial CA (CA_0) formed on the BP by the coatings was measured in sets of 3 drops on 3 BPs for 5 minutes each, with one of the drops on each set being measured during 40 minutes at a 5 second interval. Afterwards, it was let dry at room temperature for a day, the contact angle was measured (CA_{dry}).

Insulating Varnish:

Table 3.13: Initial and final contact angles (CA_0 and CA_{dry}) measured from 3 drops of insulating varnish on 3 BPs.

Sample/Drop	CA_0 (°)	CA_{dry} (°)
S1D1	130.27	-
S1D2	111.43	-
S1D3	91.09	-
Avg S1	110.93	-
S2D1	94.18	57.1
S2D2	118.53	74.7
S2D3	95.37	59.2
Avg S2	102.69	63.67
S3D1	149.89	88
S3D2	145.12	87.7
S3D3	131.45	75.7
Avg S3	121.38	83.8
Total Avg	118.59	73.73

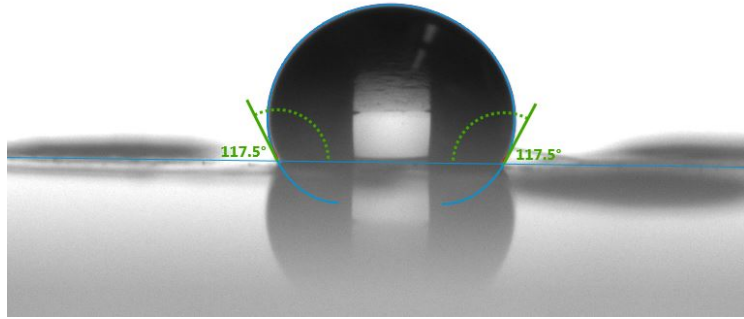


Figure 3.31: Measurement of the contact angle of a drop of varnish on a BP through the young-Laplace fitting 5 minutes after it was placed.

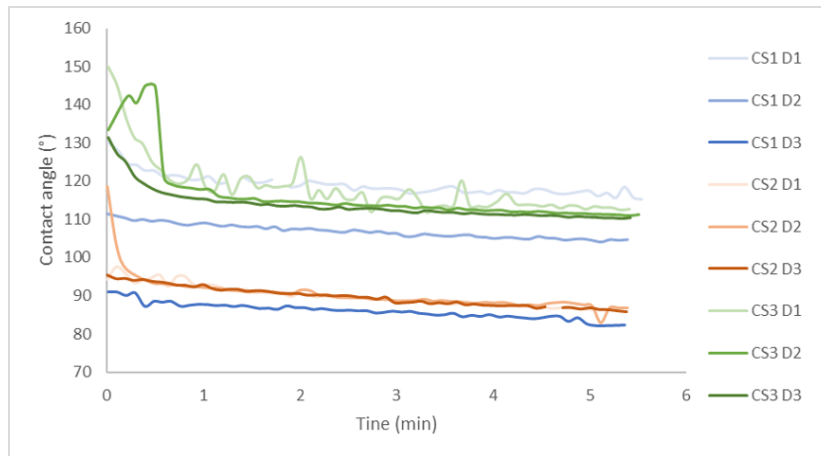


Figure 3.32: Measurement of the contact angle of a drop of insulating varnish on a BP through the young-Laplace fitting for 5 minutes after it was placed on 3 different BPs (CS1-CS3) three drops each.

Although the BP is considered as consistent, from Figure 3.32 we can see that variations occur depending on the BP porosity and surface area.

For the drops analyzed for 40 minutes (Figure 3.33), the contact angle behavior was fitted with a regression consisting of an R^2 of 0.90 or higher. In the case of varnish only one test could be fit with a logarithmic regression. It's important to consider that measuring the contact angle at minute 0 is really hard, since the change in angle is really sudden at the first seconds as it can be seen in CS3. The software also takes a few seconds to fit the contact angle, so there is a possibility that the initial contact angle was higher than the ones presented in this results. It should also be noted that due to time limitations only three out of the nine drops could be observed for 40 minutes (usually the third one). For example, if the second drop of coating sample 2 (CS2 D2 on Figure 3.32) would have been the one analyzed for 40 min, the regression

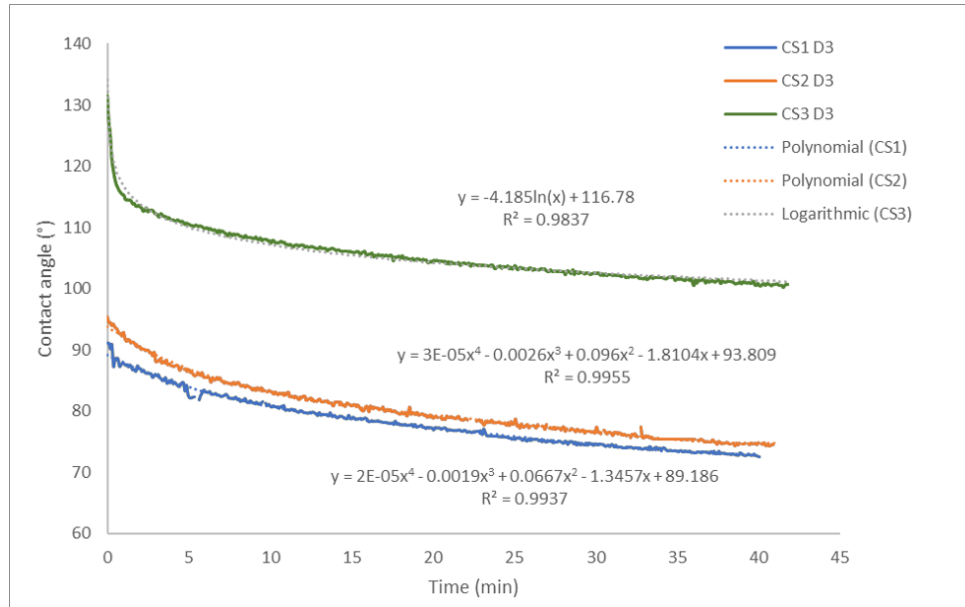


Figure 3.33: Measurement of the contact angle of a drop of insulating varnish on a BP through the young-Laplace fitting for 40 minutes after it was placed on 3 different BPs (CS1-CS3).

could have been more likely to be logarithmic.

Red Enamel:

Table 3.14: Initial and final contact angles (CA_0 and CA_{dry}) measured from 3 drops of red enamel on 3 BPs.

Sample/Drop	CA_0 (°)	CA_{dry} (°)
S1D1	134.13	105.1
S1D2	126.28	94.7
S1D3	133.36	88.5
Avg S1	131.26	96.1
S2D1	133.52	96.4
S2D2	135.05	92.6
S2D3	124.32	90.1
Avg S2	130.96	93.03
S3D1	145.61	93.7
S3D2	129.72	92.4
S3D3	124.58	93.8
Avg S3	133.30	93.3
Total Avg	131.84	94.14

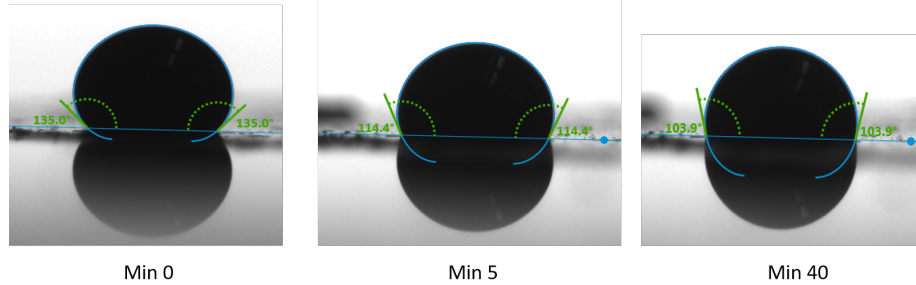


Figure 3.34: Contact angle change on a drop of red enamel on top of a BP at minutes 0, 5 and 40 from when it was dropped.

Red enamel presents a sudden decrease in the contact angle the first 5 minutes, and then a slower decrease as time passes, such as depicted in Figure 3.34.

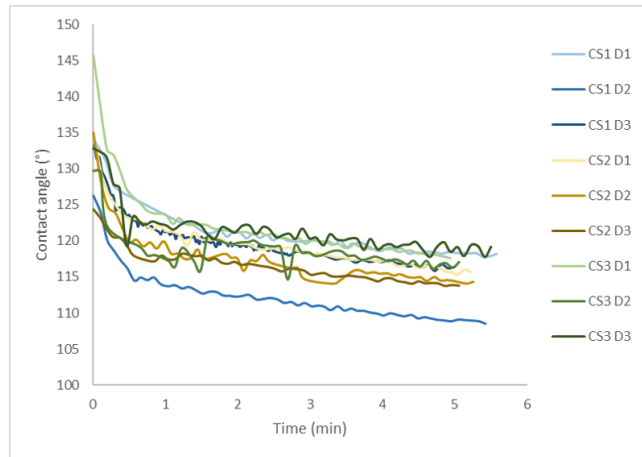


Figure 3.35: Measurement of the contact angle of a drop of red enamel on a BP through the young-Laplace fitting for 5 minutes after it was placed on 3 different BPs (CS1-CS3) three drops each.

This time, different from the insulating varnish samples not only in opacity, but also because the CA profile of all 9 drops for 5 minutes looks more similar in decrease rate (Figure 3.35).

Logarithmic behavior fitted the three of the drops tested for 40 minutes, with the lowest R^2 being 0.917 and the highest 0.987 (Figure 3.36). There was no particular reason for using drop 1 instead of drop 3 in coating sample 3.

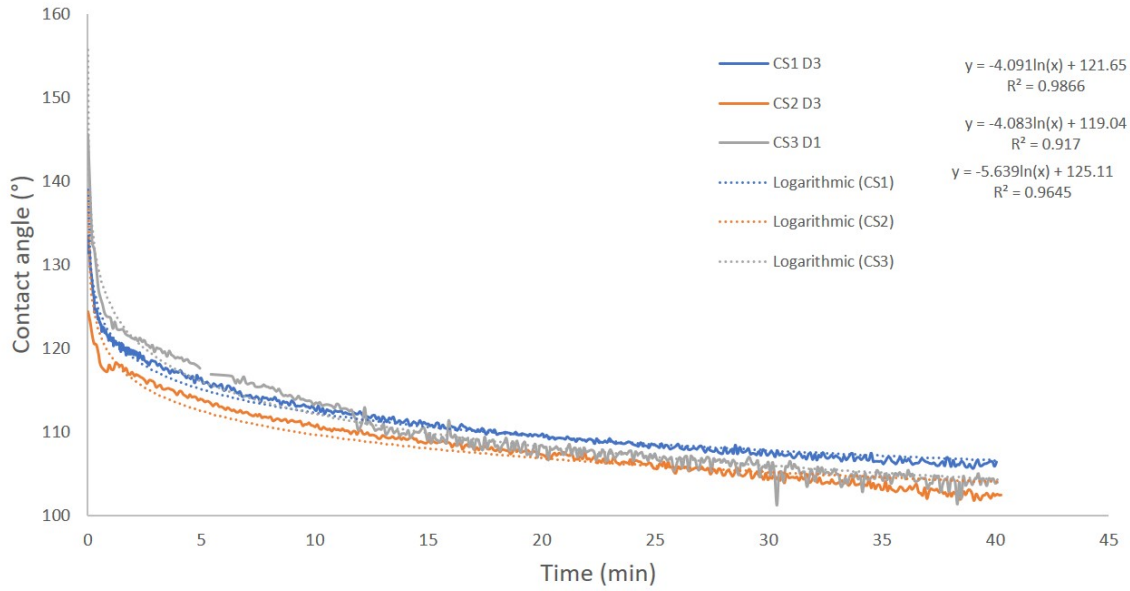


Figure 3.36: Measurement of the contact angle of a drop of red enamel on a BP through the young-Laplace fitting for 40 minutes after it was placed on 3 different BPs (CS1-CS3).

Epoxy resin:

A mixed epoxy resin with hardener was tested as soon as it was prepared. Thus, a new mixture was prepared for each drop with the same 2:1 ratio (epoxy and hardener respectively).

Table 3.15: Initial and final contact angles (CA_0 and CA_{dry}) measured from 3 drops of epoxy resin on 3 BPs.

Sample/Drop	CA_0 (°)	CA_{dry} (°)
S1D1	47.18	18.6
S1D2	40.86	18.4
S1D3	44.83	19.8
Avg S1	44.29	18.93
S2D1	35.17	29.4
S2D2	51.6	17.2
S2D3	41.05	17.2
Avg S2	42.61	21.27
S3D1	40.89	20.9
S3D2	43.96	20.6
S3D3	41.05	26.7
Avg S3	41.97	22.73
Total Avg	42.95	20.98

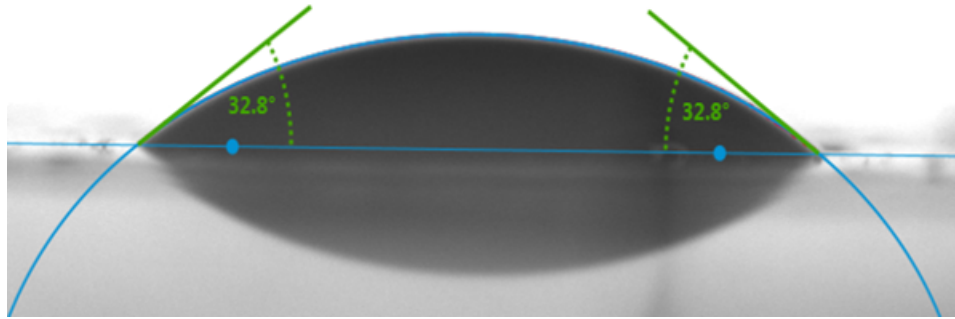


Figure 3.37: Measurement of the contact angle of a drop of epoxy resin on a BP through the young-Laplace fitting 5 minutes after it was placed.

For the epoxy resin and the insulating varnish, only images after 5 minutes were taken because of time restrictions using the equipment.

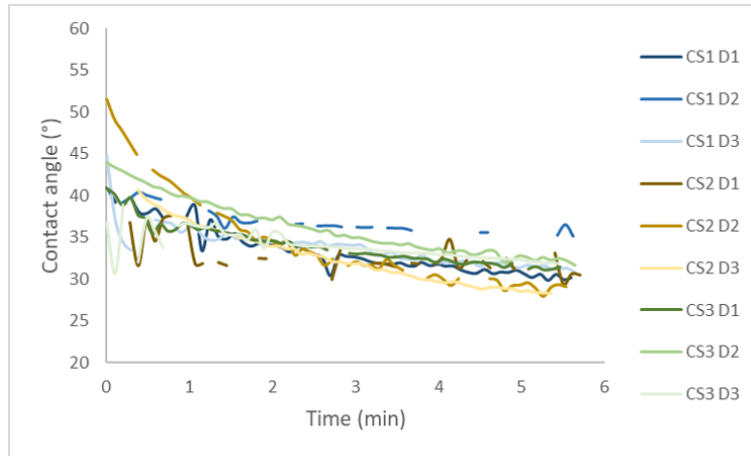


Figure 3.38: Measurement of the contact angle of a drop of epoxy resin on a BP through the young-Laplace fitting for 5 minutes after it was placed on 3 different BPs (CS1-CS3) three drops each.

Because of focus and illumination problems on the equipment, some values from Figure 3.38 don't appear, and it's because in those lapses of time the contact angle could not be measured. The contact angle profiles in all 9 drops are the most consistent out of all coatings.

Only two drops could be tested for 40 minutes with the time given on the equipment. A logarithmic equation was a good fit for coating sample 3, while coating sample 2 was polynomial since a logarithmic approach resulted in an R^2 of 0.896.

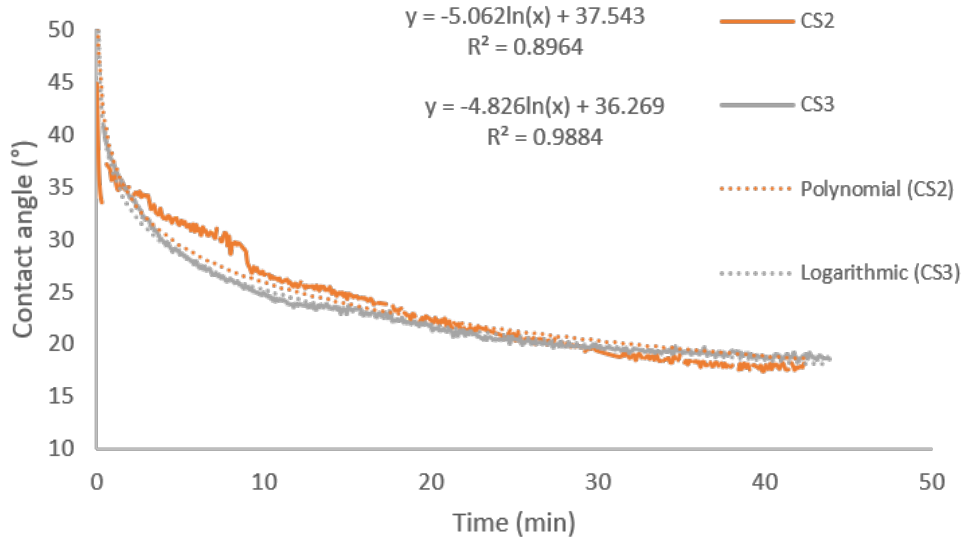


Figure 3.39: Measurement of the contact angle of a drop of epoxy resin on a BP through the young-Laplace fitting for 40 minutes after it was placed on 2 different BPs (CS2 and CS3).

All coatings:

Table 3.16: Average initial and final contact angles (CA_0 and CA_{dry}) for insulating varnish, red enamel and epoxy resin.

Coating	CA_0 (°)	CA_{dry} (°)
Insulating Varnish	118.59	73.73
Red Enamel	131.84	94.14
Epoxy Resin	42.95	20.98

Hydrophobic behavior was shown for insulating varnish and red enamel and hydrophilic for epoxy resin.

In general, logarithmic behavior was the most dominant, since it could fit at least 1 sample for all the coatings.

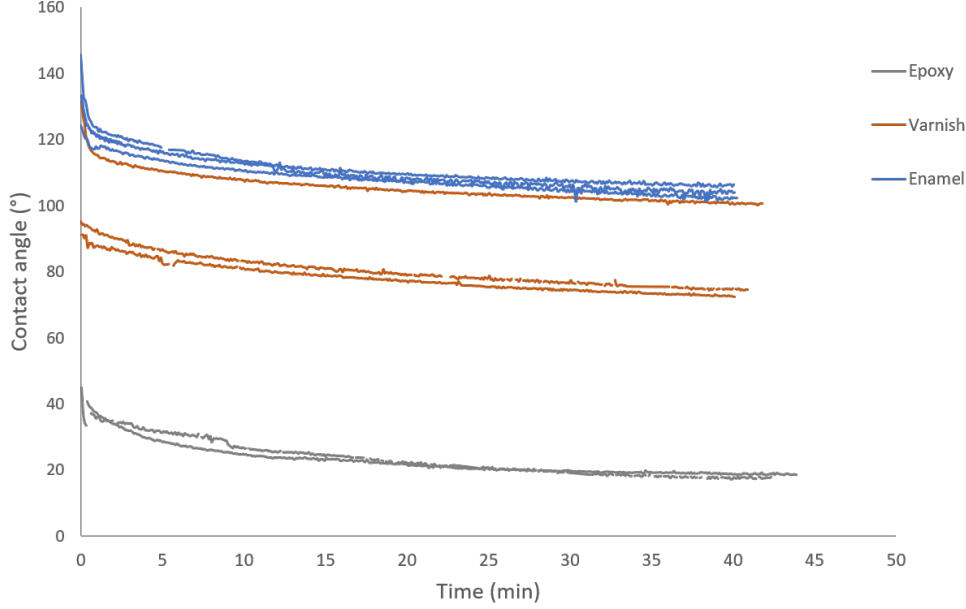


Figure 3.40: Contact angle profile for 40 minutes for all three coatings from Figures 3.33, 3.36 and 3.39.

Wetting parameters

For the calculation of the wetting parameters, it's important to consider that the BP is a structure of BP and empty space, that is filled with air or a substance applied to it. The Cassie-Baxter model [37] connects the "average" contact angle with the contact angle that would be obtained in an homogeneous structure. This approach was also tested in MWCNT CNT fibers [25].

The equation is:

$$\cos\theta_{equ} = f_s \cos\theta_{CNT} + (1 - f_s) \cos\theta_i \quad (3.4)$$

Where:

f_s is the fraction of solid/liquid interface.

θ_{equ} is the average contact angle.

θ_{CNT} is the predicted contact angle.

θ_i is the air/liquid or liquid/liquid contact angle, and is 180° or 0° respectively [51].

As mentioned before, instead of advancing and receding angle, static contact angles were measured in this study. The model was tested using the average initial contact angle, the average between the initial contact angle and the angle after 5 minutes(CA_0 -

CA_5), and the average between the initial contact angle and the dry contact angle ($\text{CA}_0-\text{CA}_{dry}$). The fraction of solid was considered as 0.695, which is 1 minus porosity obtained by DFT (Table 3.8).

Table 3.17: Contact angle calculations with the Cassie-Baxter model (Equation 3.4).

Coating/ θ_{equ}	θ_{equ} (°)	θ_{CNT} (°)
Enamel (CA_0)	131.84	121.40
Enamel (CA_0-CA_5)	123.33	110.59
Enamel ($\text{CA}_0-\text{CA}_{dry}$)	112.99	97.07
Insulating Varnish (CA_0)	118.59	104.46
Insulating Varnish (CA_0-CA_5)	109.32	92.12
Insulating Varnish ($\text{CA}_0-\text{CA}_{dry}$)	96.16	73.47
Epoxy resin (CA_0)	42.95	-
Epoxy resin (CA_0-CA_5)	36.98	-
Epoxy resin ($\text{CA}_0-\text{CA}_{dry}$)	31.97	-

The model has three main issues.

-Dynamic contact angles were measured instead of advancing and receding contact angles, thus a consideration of a different way of calculating equilibrium contact angle had to be made.

-It resulted in imaginary values when using contact angles from epoxy resin, it happens for certain combinations of porosities and contact angles.

-It gets more complex when considering that the coating are entering the BP and there is a change in f_s with time (Figure 3.41).

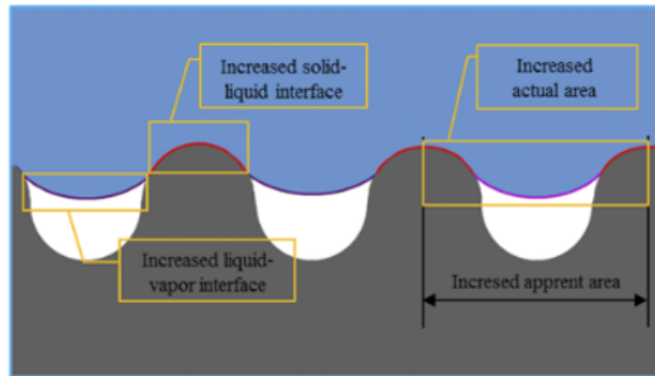


Figure 3.41: Infiltration of a liquid in the pores of a porous structure. Extracted from [11].

In the end, the θ_{CNT} obtained from using the average between the initial contact angle and the angle after 5 minutes was chosen for the calculation of the wetting

parameters, mainly because of the dominant logarithmic profile found in all coatings, where the first 5 minutes the decrease in contact angle is higher and therefore really important. For epoxy resin average initial contact angles will be directly used.

The four main wetting parameters calculated are the work of adhesion (W_a), the spreading coefficient (S), the wetting tension (ΔF) and interfacial surface tension (γ_{sl}). These parameters are obtained with the following equations:

$$W_a = \gamma_s + \gamma_l - \gamma_{sl} \quad (3.5)$$

$$S = \gamma_s - (\gamma_l + \gamma_{sl}) \quad (3.6)$$

$$\Delta F = \gamma_s - \gamma_{sl} \quad (3.7)$$

The interfacial surface tension is calculated with Young's [35] equation since the contact angle calculated through the model represents the angle in an homogeneous surface.

$$\gamma_{sl} = \gamma_s - \gamma_l \cos \theta_{CNT} \quad (3.8)$$

Where:

γ_s is the surface free energy of the BP (59.63 mJ/m₂).

γ_l is the surface tension of the coating/air interface (From Table 3.12).

The calculated parameters are shown in Table 3.18.

Table 3.18: Wetting parameters (mJ/m₂) calculated for red enamel, insulating varnish and epoxy resin.

Coating	γ_{sl}	W_a	S	ΔF
Enamel	72.43	23.59	-49.19	-12.80
Insulating Varnish	60.73	-30.85	-1.10	
Epoxy resin	32.09	-6.93	27.54	

The work of adhesion is the reversible thermodynamic work needed to separate the interface from the equilibrium state of two phases to a separation distance of infinity. The higher " W_a ", the higher the adhesion, red enamel is the one with higher adhesion. For the fiber we want high adhesion as long as it doesn't affect too negatively the conductivity.

The spreading coefficient is a measure of the tendency of a liquid phase to spread on another phase, and is related to how much it wets the surface. Epoxy resin had the only positive spreading coefficient, and it's higher wetting is expected since low contact angles were obtained in comparison to the other 2 coatings. The higher the spreading coefficient the easier it is to apply and cover the fiber with the coating.

Wetting tension is the maximum liquid surface tension that will spread, rather than bead up, on the film surface, estimating a film's surface energy. Epoxy resin has the highest value, since it's directly related to the spreading coefficient and general wetting of the BP. That is why maximum wetting tension is also preferred for the coating of fibers.

Interfacial tension is the work which must be expended to increase the size of the interface between two adjacent phases that do not mix completely with one another. Optimal coating is achieved with minimum interfacial tension, where epoxy resin had the lowest interfacial tension.

Overall epoxy resin had better wetting results, and red enamel had better adhesion results (insulating varnish results were close). The next important test is to know how will that affect conductivity.

Buckypaper-coating interface

To have a better understanding of the physical interfacial interactions, SEM images of the interface formed between the Bucky Paper and all four coatings were taken at different magnitudes. Due to the insulating properties of the coatings, the quality at which the interface is seen is low. Thus, getting new images with a gold sputtering on the surface is suggested.

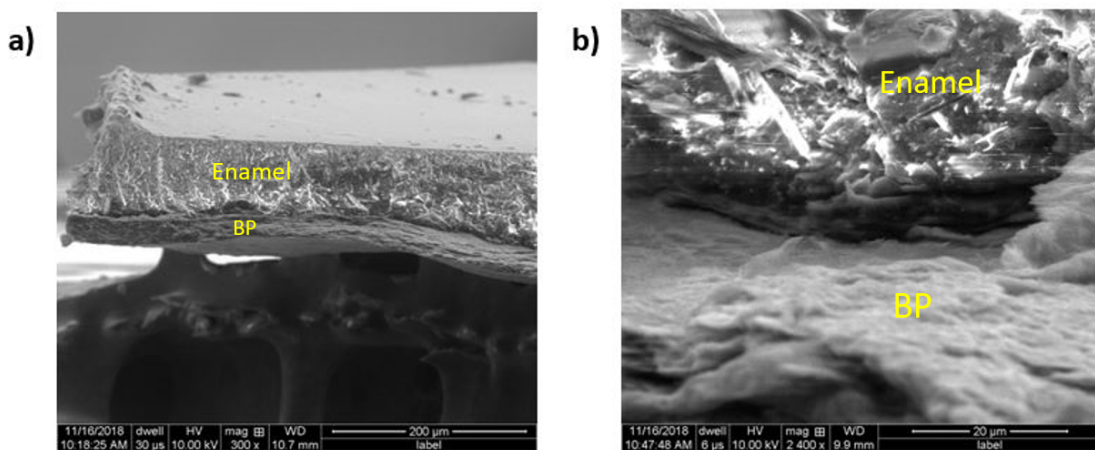


Figure 3.42: Image of the interface formed from a BP coated with red enamel (coated side is the upper layer) at 300x (a) and 2400x (b) magnitudes.

For the enamel not much could be seen from the images, they looked like two immis-

cible materials, which would be in agreement with the low wettability.

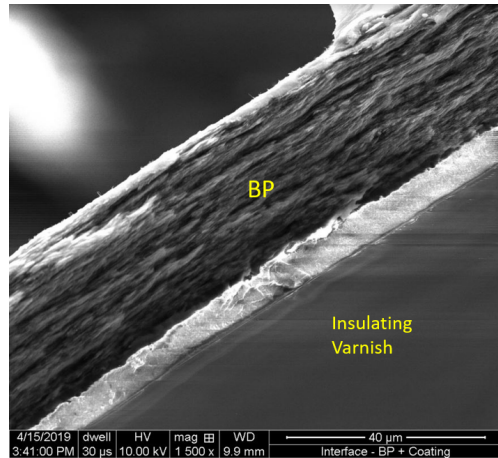


Figure 3.43: Image of the interface formed from a BP coated with insulating varnish (coated side is the lower layer) at a 1500x magnitude.

Varnish-BP interface was difficult to see, 1500x was the most zoomed clear image obtained. Not much can be said other than no macroscopic penetration into the BP was observed.

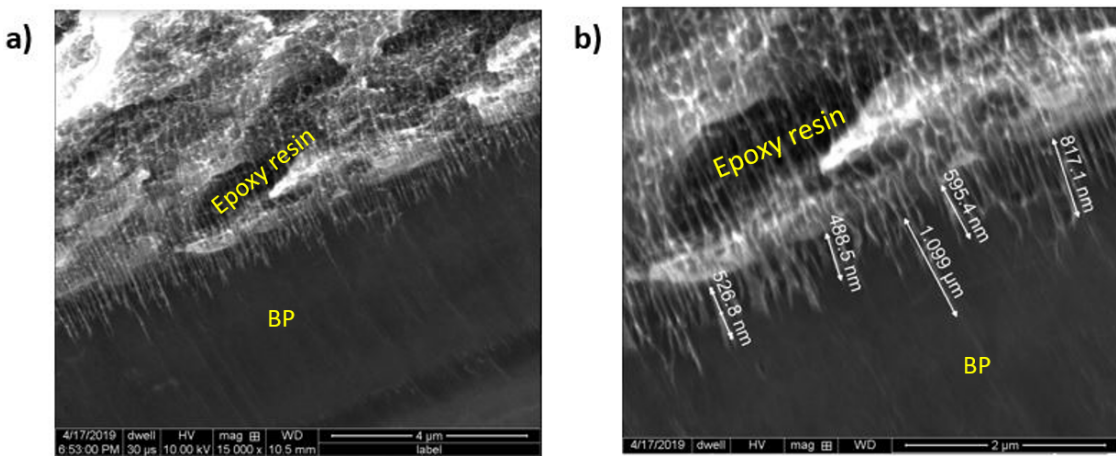


Figure 3.44: Image of the interface formed from a BP coated with epoxy resin (coated side is the upper layer) at 15000x (a) and 30000x (b) magnitudes.

Figure 3.44 was the most interesting, a maximum penetration of $1 \mu\text{m}$ into the BP was observed. The higher wettability helped it to get into the pores, however, the more it penetrates the more it can affect conductivity. This image also shows that pores inside the BP could have more of a cylindrical shape than a spherical one.

For polyethylene wax, not having the wetting and adhesion parameters and having low image quality because of the low conductivity and no gold sputtering, not much can be said for this coating, other than no macroscopic adhesion was observed.

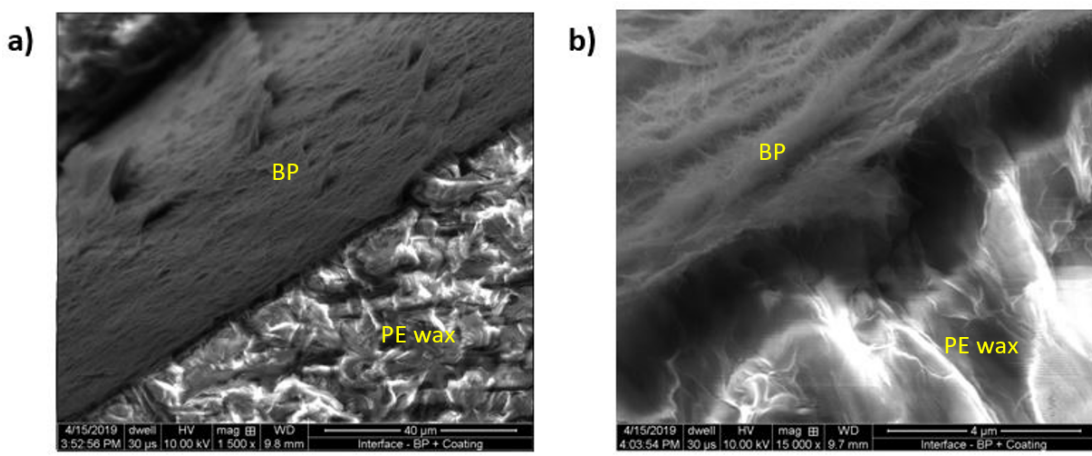


Figure 3.45: Image of the interface formed from a BP coated with Polyethylene wax (coated side is the lower layer) at 1500x (a) and 15000x (b) magnitudes.

3.1.5 Conductivity

The setup consists of 12mm x 12mm BP squares, with silver paint on the edges leading to a copper tape, where measurements are taken. In total 15 samples were prepared (Figure 3.46)



Figure 3.46: Conductivity measurement setup before coating.

After the resistances were measured in sets of 3, samples were coated with the four coating materials. In order to have an even coating, three drops of the coating were deposited in the center of the sample (Figure 3.47) and then spread with a razor in a cross pattern (Figure 3.48), leaving the edges uncoated. Three uncoated buckypapers were used as control samples.

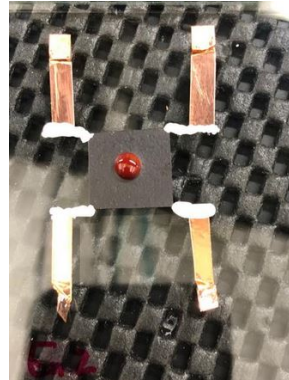


Figure 3.47: Buckypaper connected to copper tape through silver paint. The Buckypaper has 3 fused drops of red enamel on the center.

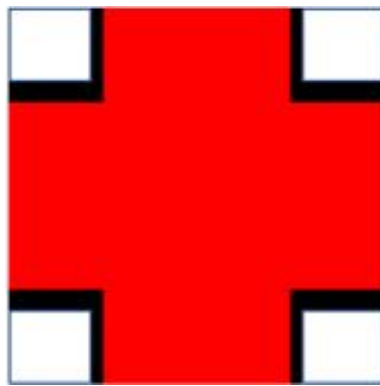


Figure 3.48: Representation of the cross pattern in which the coating was applied.

Each coating was cured as indicated in Table 3.19.

Table 3.19: Curing conditions for all coatings.

Coating Time	Temperature
Glyptal® 1202 Insulating Varnish 3 hours	100°C
Glyptal® 1201 Red Enamel 3 hours	100°C
635 Thin Epoxy Resin 5 hours	40°C
Epolene® wax 8 hours	25°C

Resistivity values were obtained for days 1, 4 and 7. Resistivity was then converted into conductivity (conductivity is the inverse of resistivity), and sample values were averaged.

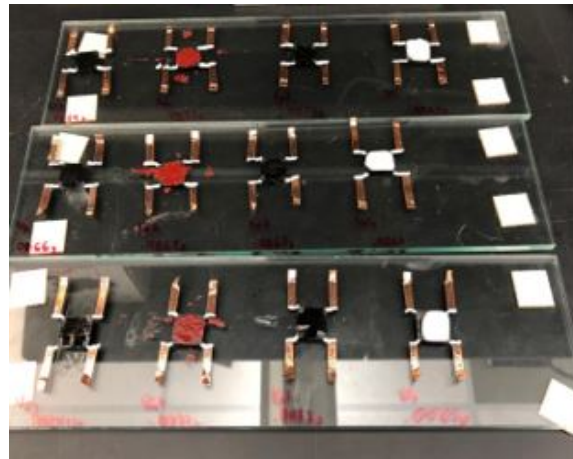


Figure 3.49: Conductivity measurement setup after coating.

The resistivity of the samples that were coated (Table 3.20) and the control samples that were not coated (Table 3.21) was calculated from the results of the resistance measurements, and from resistivity, conductivity was obtained.

Table 3.20: Resistivities (ρ) of samples that were coated, where day 0 is the measurement for the uncoated sample and from day 1 on is the coated and cured sample. S1, S2 and S3 are samples 1, 2 and 3 of each coating.

Coating	ρ Day 0 (Ωm)	ρ Day 1 (Ωm)	ρ Day 4 (Ωm)	ρ Day 7 (Ωm)
Varnish S1	4.45×10^{-5}	5.53×10^{-5}	5.11×10^{-5}	4.96×10^{-5}
Varnish S2	3.95×10^{-5}	4.52×10^{-5}	4.26×10^{-5}	4.15×10^{-5}
Varnish S3	3.64×10^{-5}	4.53×10^{-5}	4.28×10^{-5}	4.18×10^{-5}
Varnish Avg	4.01×10^{-5}	4.86×10^{-5}	4.55×10^{-5}	4.43×10^{-5}
Epoxy S4	3.49×10^{-5}	9.88×10^{-5}	9.09×10^{-5}	8.74×10^{-5}
Epoxy S5	3.48×10^{-5}	12×10^{-5}	11.2×10^{-5}	10.8×10^{-5}
Epoxy S6	4.08×10^{-5}	13.8×10^{-5}	12.8×10^{-5}	12.4×10^{-5}
Epoxy Avg	3.68×10^{-5}	11.9×10^{-5}	11.1×10^{-5}	10.6×10^{-5}
Enamel S7	3.35×10^{-5}	3.93×10^{-5}	3.68×10^{-5}	3.59×10^{-5}
Enamel S8	3.58×10^{-5}	4.47×10^{-5}	4.23×10^{-5}	4.13×10^{-5}
Enamel S9	3.90×10^{-5}	4.72×10^{-5}	4.45×10^{-5}	4.34×10^{-5}
Enamel Avg	3.61×10^{-5}	4.38×10^{-5}	4.12×10^{-5}	4.02×10^{-5}
Wax S10	3.80×10^{-5}	7.04×10^{-5}	6.95×10^{-5}	6.92×10^{-5}
Wax S11	3.93×10^{-5}	6.64×10^{-5}	6.56×10^{-5}	6.55×10^{-5}
Wax S12	4.11×10^{-5}	6.56×10^{-5}	6.47×10^{-5}	6.21×10^{-5}
Wax Avg	3.95×10^{-5}	6.75×10^{-5}	6.66×10^{-5}	6.56×10^{-5}

Table 3.21: Resistivities (ρ) of uncoated control samples.

Sample	ρ Day 1 (Ωm)	ρ Day 4 (Ωm)	ρ Day 7 (Ωm)
Control S1	4.20×10^{-5}	3.88×10^{-5}	3.65×10^{-5}
Control S2	4.40×10^{-5}	3.69×10^{-5}	3.44×10^{-5}
Control S3	4.66×10^{-5}	3.84×10^{-5}	3.57×10^{-5}
Control Avg	4.42×10^{-5}	3.81×10^{-5}	3.55×10^{-5}

For all coatings, there is a sudden decrease in conductivity from day 0 to day 1. However, the following days conductivity increases (Table 3.23). To discard that it was only due to the coating effect, the conductivity behavior of uncoated BP was also analyzed (Table 3.22). The control samples also experienced an increase in conductivity up to day 7 (24.48%), which means something else is also making the conductivity go up.

From day 0 to day 1, coating with epoxy resin resulted in the highest conductivity sudden decrease (-68.72%), and that can be supported with the SEM images observed at the interface (Figure 3.44), where the coating seems to penetrate into the pores of the BP.

The second highest conductivity increase in the same time-lapse happened in the wax coating (-41.37%). From the SEM images (3.45), there is spots when one can say penetration can be somewhat interpreted, however, due to the insulating properties, these spots are not as clear on the image as in the epoxy ones.

The insulating varnish and the red enamel were the two best performance coatings in terms of conductivity, with decreases of 17.17% and 17.49% respectively, that by day 7 was a decrease of only 9.31% and 10.20%.

Table 3.22: Conductivities (σ) of uncoated control samples.

Sample	σ Day 1(S/m)	σ Day 4(S/m)	σ Day 7(S/m)
Control S1	2.38×10^4	2.57×10^4	2.74×10^4
Control S2	2.27×10^4	2.71×10^4	2.91×10^4
Control S3	2.15×10^4	2.60×10^4	2.80×10^4
Control Avg	2.27×10^4	2.63×10^4	2.82×10^4

Table 3.23: Conductivities (σ) of samples that were coated, where day 0 is the measurement for the uncoated sample and from day 1 on is the coated and cured sample.

Coating	σ Day 0(S/m)	σ Day 1(S/m)	σ Day 4(S/m)	σ Day 7(S/m)
Varnish S1	2.25x10 ⁴	1.81x10 ⁴	1.96x10 ⁴	2.01x10 ⁴
Varnish S2	2.53x10 ⁴	2.21x10 ⁴	2.35x10 ⁴	2.41x10 ⁴
Varnish S3	2.75x10 ⁴	2.21x10 ⁴	2.33x10 ⁴	2.39x10 ⁴
Varnish Avg	2.51x10⁴	2.08x10⁴	2.21x10⁴	2.27x10⁴
Epoxy S4	2.87x10 ⁴	1.01x10 ⁴	1.10x10 ⁴	1.14x10 ⁴
Epoxy S5	2.88x10 ⁴	0.83x10 ⁴	0.89x10 ⁴	0.92x10 ⁴
Epoxy S6	2.45x10 ⁴	0.73x10 ⁴	0.78x10 ⁴	0.81x10 ⁴
Epoxy Avg	2.73x10⁴	8.56x10³	9.23x10³	9.58x10³
Enamel S7	2.99x10 ⁴	2.54x10 ⁴	2.72x10 ⁴	2.78x10 ⁴
Enamel S8	2.79x10 ⁴	2.23x10 ⁴	2.37x10 ⁴	2.42x10 ⁴
Enamel S9	2.57x10 ⁴	2.12x10 ⁴	2.25x10 ⁴	2.30x10 ⁴
Enamel Avg	2.78x10⁴	2.30x10⁴	2.44x10⁴	2.50x10⁴
Wax S10	2.63x10 ⁴	1.42x10 ⁴	1.44x10 ⁴	1.45x10 ⁴
Wax S11	2.55x10 ⁴	1.51x10 ⁴	1.52x10 ⁴	1.53x10 ⁴
Wax S12	2.43x10 ⁴	1.53x10 ⁴	1.54x10 ⁴	1.61x10 ⁴
Wax Avg	2.54x10⁴	1.48x10⁴	1.50x10⁴	1.53x10⁴

Table 3.24: Average conductivity change ($\Delta \sigma$) of each set of 3 samples from their first day of measurement (Day 0).

Sample	$\Delta \sigma$ Day 0-Day 1	$\Delta \sigma$ Day 0-Day 4	$\Delta \sigma$ Day 0-Day 7
Varnish	-17.17%	-11.74%	-9.31%
Epoxy	-68.72%	-66.28%	-64.99%
Enamel	-17.49%	-12.30%	-10.20%
Wax	-41.37%	-40.61%	-39.59%
Control	-	16.09%	24.48%

Chapter 4

Conclusions

Using the BP as an approach of CNT fibers was justified through the results showing similar physisorption curves, porosity and surface as MWCNT fibers from different studies.

When looking for the optimal coating, both adhesion and wettability are important. However too much adhesion or wettability can also worsen the electrical performance of the wire. This was proven since epoxy resin resulted in better wettability behavior while red enamel and insulating varnish had better adhesion, the difference was in the enamel and varnish having the lowest conductivity decrease after 1 day (17.49% and 17.17%. respectively) compared to the 68.72% from epoxy. The decision of what the more optimal coating is depends on the final required electrical and mechanical performance for an specific application.

The main contribution of this work is using a cheaper and easier to make CNT structure as an approach to a CNT fiber, and at the same time linking the wetting aspects with the electrical performance to propose an easier and cheaper protocol for the testing of different coatings materials for the development of CNT electrical wires for different applications without wasting as much CNT fibers.

A more detailed characterization such as XPS deconvolution would help in determining with more certainty the factors that caused variations such as the high and low contact angles of water obtained. More raman spectroscopy data for chirality determination is also important for characterization of the BP since chirality is really important for inherent electrical conductivity of the CNTs. Mechanical tests could also be implemented in the future.

Many assumptions that had to be made such as using the sessile drop method instead of dynamic contact angle measurements could be optimized in the future, such as determination of θ_{equ} . A methodology to obtain the equivalent contact angle on homogeneous surface that considers the changing solid/liquid fraction because of penetration of the liquid on the pores could also be considered in the future.

Bibliography

- [1] Thermoscientific, “Carbon,” 2019. Last accessed 21 October 2019.
- [2] Thermoscientific, “Oxygen,” 2019. Last accessed 21 October 2019.
- [3] Thermoscientific, “Nitrogen,” 2019. Last accessed 21 October 2019.
- [4] A. Kozbial, Z. Li, C. Conaway, R. McGinley, S. Dhingra, V. Vahdat, F. Zhou, B. D’ Urso, H. Liu, and L. Li, “Study on the surface energy of graphene by contact angle measurements,” *Langmuir*, vol. 30, no. 28, pp. 8598–8606, 2014. PMID: 24983409.
- [5] M. S. Dresselhaus, A. Jorio, M. Hofmann, G. Dresselhaus, and R. Saito, “Perspectives on carbon nanotubes and graphene raman spectroscopy,” *Nano Letters*, vol. 10, no. 3, pp. 751–758, 2010.
- [6] M. Thommes, K. Kaneko, A. Neimark, J. Olivier, F. Rodriguez-Reinoso, J. Rouquerol, and K. Sing, “Physisorption of gases, with special reference to the evaluation of surface area and pore size distribution (iupac technical report),” *Pure and Applied Chemistry*, vol. 87, 01 2015.
- [7] D. Liviu, A. Popescu, I. Zgura, N. Preda, and I. Mihailescu, *Wettability of Nanosstructured Surfaces*, pp. 207–252. 12 2015.
- [8] F. Ferreira, W. Franceschi, B. Menezes, F. Brito, K. Lozano, A. Coutinho, L. Cividanes, and G. Thim, “Dodecylamine functionalization of carbon nanotubes to improve dispersion, thermal and mechanical properties of polyethylene based nanocomposites,” *Applied Surface Science*, vol. 410, pp. 267 – 277, 2017.
- [9] J. Qiu, J. Terrones, J. J. Vilatela, M. E. Vickers, J. A. Elliott, and A. H. Windle, “Liquid infiltration into carbon nanotube fibers: effect on structure and electrical properties.,” *ACS nano*, vol. 7, no. 10, pp. 8412,8422, 2013-10-22.
- [10] S. Gupta, F. Bosco, and R. Batra, “Wall thickness and elastic moduli of single-walled carbon nanotubes from frequencies of axial, torsional and inextensional modes of vibration,” *Computational Materials Science*, vol. 47, no. 4, pp. 1049 – 1059, 2010.

- [11] K. Grundke, T. Hoffmann, T. Gietzelt, H. Jacobasch, D. Kwok, and A. Neumann, “Wetting measurements on smooth, rough and porous solid surfaces,” *Progress in Colloid and Polymer Science*, vol. 101, pp. 58–68, 12 2007.
- [12] R. Chavan, U. Desai, P. Mhatre, and R. Chinchole, “A review: Carbon nanotubes,” *International Journal of Pharmaceutical Sciences Review and Research*, vol. 13, pp. 125–134, 2012.
- [13] D. E. Tsentalovich, R. J. Headrick, F. Mirri, J. Hao, N. Behabtu, C. C. Young, and M. Pasquali, “Influence of carbon nanotube characteristics on macroscopic fiber properties.,” *ACS applied materials interfaces*, vol. 9, no. 41, pp. 36189,36198, 2017-10-18.
- [14] S. Ayyagari, M. Al-Haik, and V. Rollin, “Mechanical and electrical characterization of carbon fiber/bucky paper/zinc oxide hybrid composites,” *C*, vol. 4, no. 1, 2018-01-01.
- [15] K. Chu, D. Kim, Y. Sohn, S. Lee, C. Moon, and S. Park, “Electrical and thermal properties of carbon-nanotube composite for flexible electric heating-unit applications,” *IEEE Electron Device Letters*, vol. 34, no. 5, pp. 668,670, 2013-05.
- [16] A. Zubair, D. E. Tsentalovich, C. C. Young, M. S. Heimbeck, H. O. Everitt, M. Pasquali, and J. Kono, “Carbon nanotube fiber terahertz polarizer,” *Applied Physics Letters*, vol. 108, no. 14, 2016-04-04.
- [17] S. H. Kim, C. S. Haines, N. Li, K. J. Kim, T. J. Mun, C. Choi, J. Di, Y. J. Oh, J. P. Oviedo, J. Bykova, S. Fang, N. Jiang, Z. Liu, R. Wang, P. Kumar, R. Qiao, S. Priya, K. Cho, M. Kim, M. S. Lucas, L. F. Drummy, B. Maruyama, D. Y. Lee, X. Lepró, E. Gao, D. Albarq, R. Ovalle-Robles, S. J. Kim, and R. H. Baughman, “Harvesting electrical energy from carbon nanotube yarn twist.,” *Science (New York, N.Y.)*, vol. 357, no. 6353, pp. 773,778, 2017-08-25.
- [18] H. M. Faraby, A. M. Rao, and P. R. Bandaru, “Modeling high energy density electrical inductors operating at thz frequencies based on coiled carbon nanotubes,” *IEEE Electron Device Letters*, vol. 34, no. 6, pp. 807,809, 2013-06.
- [19] S. Aldrich, “Carbon nanotube, single-walled 98% semiconducting,” 2019. Last accessed 23 September 2019.
- [20] S. Aldrich, “Carbon nanotube, single-walled 98% metallic,” 2019. Last accessed 23 September 2019.
- [21] Q. Lu, G. Keskar, R. Ciocan, R. Rao, R. B. Mathur, A. M. Rao, and L. L. Larcom, “Determination of carbon nanotube density by gradient sedimentation,” *The Journal of Physical Chemistry B*, vol. 110, no. 48, pp. 24371–24376, 2006.
- [22] J. R. Rumble, *CRC Handbook of chemistry and physics*. Boca Raton CRC Press, Taylor et Francis Group.

- [23] Y. Zhao, J. Wei, R. Vajtai, P. M. Ajayan, and E. V. Barrera, “Iodine doped carbon nanotube cables exceeding specific electrical conductivity of metals.,” *Scientific reports*, vol. 1, no. 1, pp. 83,83, 2011-01-01.
- [24] I. C. S. Group, “Copper: Preliminary data for march 2019,” June 2019. <https://> Last accessed 23 September 2019.
- [25] L. Zhang, J. Wang, C. Fuentes, D. Zhang, A. Van Vuure, J. Seo, and D. Seveno, “Wettability of carbon nanotube fibers,” *Carbon*, vol. 122, 2017-10-01.
- [26] D. Janas, A. P. Herman, S. Boncel, and K. K. Koziol, “Iodine monochloride as a powerful enhancer of electrical conductivity of carbon nanotube wires,” *Carbon*, vol. 73, pp. 225 – 233, 2014.
- [27] S. Hosseiniinasab, N. Faucheuix, G. Soucy, and J. R. Tavares, “Full range of wettability through surface modification of single-wall carbon nanotubes by photo-initiated chemical vapour deposition,” *Chemical Engineering Journal*, vol. 325, pp. 101 – 113, 2017.
- [28] J. R. Ferraro, K. Nakamoto, and C. W. Brown, “Chapter 1 - basic theory,” in *Introductory Raman Spectroscopy (Second Edition)* (J. R. Ferraro, K. Nakamoto, and C. W. Brown, eds.), pp. 1 – 94, San Diego: Academic Press, second edition ed., 2003.
- [29] A. Ferrari and J. Robertson, “Raman spectroscopy of amorphous, nanostructured, diamond-like carbon, and nanodiamond,” *Philosophical transactions. Series A, Mathematical, physical, and engineering sciences*, vol. 362, pp. 2477–512, 12 2004.
- [30] M. Dresselhaus, G. Dresselhaus, R. Saito, and A. Jorio, “Raman spectroscopy of carbon nanotubes,” *Physics Reports*, vol. 409, no. 2, pp. 47 – 99, 2005.
- [31] M. Milnera, J. Kürti, M. Hulman, and H. Kuzmany, “Periodic resonance excitation and intertube interaction from quasicontinuous distributed helicities in single-wall carbon nanotubes,” *Physical review letters*, vol. 84, pp. 1324–7, 03 2000.
- [32] K.-i. Sasaki, R. Saito, G. Dresselhaus, M. S. Dresselhaus, H. Farhat, and J. Kong, “Curvature-induced optical phonon frequency shift in metallic carbon nanotubes,” *Physical Review B*, vol. 77, Jun 2008.
- [33] S. Brunauer, P. H. Emmett, and E. Teller, “Adsorption of gases in multimolecular layers,” *Journal of the American Chemical Society*, vol. 60, no. 2, pp. 309–319, 1938.
- [34] A. materials, “Pore size analysis by gas adsorption and the density functional theory,” 2010. Last accessed 15 Januery 2020.

- [35] Y. Thomas, “An essay on the cohesion of fluids,” *Philosophical Transactions of the Royal Society of London*, pp. 65–87, 1805.
- [36] R. N. Wenzel, “RESISTANCE OF SOLID SURFACES TO WETTING BY WATER,” *Industrial & Engineering Chemistry*, vol. 28, pp. 988–994, aug 1936.
- [37] A. B. D. Cassie and S. Baxter, “Wettability of porous surfaces,” *Trans. Faraday Soc.*, vol. 40, pp. 546–551, 1944.
- [38] N. Patankar, “On the modeling of hydrophobic contact angles on rough surfaces,” *Langmuir*, vol. 19, 01 2003.
- [39] J. Bico, U. Thiele, and D. Quéré, “Wetting of textured surfaces,” *Colloids and Surfaces A: Physicochemical and Engineering Aspects*, vol. 206, no. 1, pp. 41 – 46, 2002.
- [40] N. I. of Standards and Technology, “Resistivity and hall measurements,” 2019. Last accessed 30 September 2019.
- [41] E.-P. S. Costa, “Characterization of carbon nanotubes by raman spectroscopy,” *Materials Science-Poland*, vol. 26, no. 41, pp. 433–441, 2008.
- [42] P. Monson, “Understanding adsorption/desorption hysteresis for fluids in mesoporous materials using simple molecular models and classical density functional theory,” *Microporous and Mesoporous Materials*, vol. 160, pp. 47 – 66, 2012.
- [43] M. Thommes and K. Cychosz, “Physical adsorption characterization of nanoporous materials: Progress and challenges,” *Adsorption*, vol. 20, 02 2014.
- [44] J. Landers, G. Gor, and A. Neimark, “Density functional theory methods for characterization of porous materials,” *Colloids and Surfaces A: Physicochemical and Engineering Aspects*, vol. 437, pp. 3–32, 1 2013.
- [45] NanoArmor, “Single-walled carbon nanotubes - 90%swnts (95%cnts),” 2019. Last accessed 30 September 2019.
- [46] E. W. Washburn, “The dynamics of capillary flow,” *Phys. Rev.*, vol. 17, pp. 273–283, Mar 1921.
- [47] D. K. Owens and R. C. Wendt, “Estimation of the surface free energy of polymers,” *Journal of Applied Polymer Science*, vol. 13, no. 8, pp. 1741–1747, 1969.
- [48] R. J. Good and L. A. Girifalco, “A theory for estimation of surface and interfacial energies. iii. estimation of surface energies of solids from contact angle data,” *The Journal of Physical Chemistry*, vol. 64, no. 5, pp. 561–565, 1960.
- [49] E. Dujardin, T. W. Ebbesen, A. Krishnan, and M. M. J. Treacy, “Wetting of single shell carbon nanotubes,” *Advanced Materials*, vol. 10, no. 17, pp. 1472–1475, 1998.

- [50] Krüss, “Determining the surface tension of liquids by measurements on pendant drops.,” 2010. Last accessed 26 Februrary 2020.
- [51] G. McHale, “Cassie and wenzel: Were they really so wrong?,” *Langmuir*, vol. 23, no. 15, pp. 8200–8205, 2007. PMID: 17580921.